



International Journal of Engineering and Geosciences





*International Journal of Engineering and Geosciences (IJEG),
Vol; 3; , Issue; 1, pp. 001-005, February, 2018, ISSN 2548-0960, Turkey,
DOI: [10.26833/ijeg.333686](https://doi.org/10.26833/ijeg.333686)*

DETECTION OF FOOT BONE ANOMALY USING MEDICAL PHOTOGRAMMETRY

Catal Reis, H. *

Department of Geomatics, Faculty of Engineering and Natural Sciences, Gumushane University, Gumushane, 29000,
Turkey

(hcatal@gumushane.edu.tr, hatice.catal@yahoo.com.tr)

ORCID 0000-0003-2696-2446

*Corresponding Author, Received: 09/08/2017, Accepted: 06/09/2017

ABSTRACT: Photogrammetry has been used for medical diagnostic and treatment. Mostly used medical photogrammetric techniques are Ultrasound, Computed Tomography (CT) and Magnetic Resonance Imaging (MRI) images. CT and MRI are the most effective method for the early detection of foot and ankle anomaly. Researchers have been developing various methods to detect anomaly. Many image segmentation techniques are available in the literature. Computer Aided Diagnosing (CAD) system has been proposed in this study for detection of foot bone anomaly by the analysis of CT images. In this study, a segmentation based on edge detection method is proposed for the classification of anomaly in foot CT images. Edge detection algorithms are the most commonly used techniques in image processing for edge detection. Canny edge detector is evaluated in this study.

In this study, “.dicom” medical image standard format and ten male patient’s foot CT images (245 images and 50 test data) are used. The used parameters are detector collimation of 64 mm, scanning thickness of 1-5 mm, and pixel sizes of 512x512 in radiometric resolution of 16 bits’ gray levels.

The proposed method consists of five major steps: (i) calculating the horizontal & vertical gradient, (ii) determining gradient magnitude and gradient direction, (iii) applying non-maximal suppression, (iv) computing high and low thresholds, (v) hysteresis thresholding are applied to the multi-detector computed tomography to detect the bone anomaly.

In this study, automatic edge-based digital image processing techniques are applied to detect of foot bone anomaly. The proposed canny segmentation method enables users segment anomaly in MDCT of foot very quickly and efficiently. The results demonstrate that the proposed segmentation method is effective for segmenting anomaly. The proposed method obtains satisfactory performances in terms of accuracy and F-measure the area under Receiver Operating Characteristic curve (ROC curve (AUC)). The proposed segmentation method achieves an accuracy of 0.86 and F-measure of 0.92, respectively.

The purpose of our study is to detect the anomaly of the foot and it was the simplest and less time consuming process.

Keywords: *Medical Photogrammetry, Medical Image Processing, Segmentation, Anomaly, CT*

1. INTRODUCTION

The medical photogrammetry, being non-invasive methods are, apart from their geomatics applications, very convenient and precise tools for measuring medical forms and functions, as well as shapes, locations and three-dimensional of anatomic organs, area, volume and their changes in time. Medical photogrammetry generally uses medical images. Medical imaging is varied: computed tomography (CT), magnetic resonance imaging (MRI), ultrasound, angiography, and others. CT that used in this study, becomes a key tool for any theoretical framework and applied examination. In medical imaging, many applications require the classification of images in different anatomical regions: bone, muscles, organs and detection of pathological areas, such as tumors or anomaly lesions.

Anomaly lesions of the foot and ankle are rare (Foo and Raby, 2005; Bakotic and Huvos, 2001; Mascard et al., 2017). Several diagnosis methods have been proposed for anomaly/tumor detection. MR and CT imaging methods are commonly used for diagnosis (Hasbek et al., 2013). However, these imaging and diagnosis systems are not sufficient alone to meet accurate and reliable results. Second opinion is essential to avoid inadequacies and additional requirements of imaging systems and technicians and physicians failures. Therefore Computer Aided Diagnosing (CAD) is proposed for diagnosis and treatment (Lodwick et al., 1963; Toriwaki et al., 1973). CAD is applied widely in the detection and diagnosis of many types of abnormalities in medical images obtained in examinations by use of different imaging techniques (Giger et al., 2000). CAD is a term that established by taking into account equally the roles of physicians and software, whereas automated computer diagnosis is a concept based on computer algorithms only (Doi, 2007).

Edge detection can be used in many fields such as in medical field. Canny has proposed a new method of edge detecting (Canny, 1983; Canny 1986), which is the best one to step-type edge which is influenced by noise. Canny edge detection algorithms are the most commonly used techniques in image processing for edge detection. Canny edge detector is evaluated in this study.

In this study, most convenient segmentation method has been searched to detect anomaly of the foot in CT images. Matlab platform has been used for anomaly segmentation.

The manuscript of the paper is organized as follows: 1. Introduction, 2. Segmentation, 3. Bone anomaly, 4. Methods, 5. Conclusions. These five steps are described in more details as the following sections.

2. SEGMENTATION

The image preprocessing is an important step before doing further the segmentation of anomaly. Image noise is removed before segmentation. Segmentation is the most important part in image processing (Yogamangalam and Karthikeyan, 2013). The accurate segmentation of foot anomaly is an essential step for

subsequent feature detection step. Image segmentation is the process clustering or dividing an image into multiple homogeneous regions and simplifying and obtaining searched object from original image (Kizilkaya, 2008).

Image segmentation algorithms generally are based on one of two properties of intensity values: similarity and discontinuity. Edge detection is the most common approach for detecting meaningful discontinuities in gray scale by far (Gonzalez and Woods, 2007).

Edge detection defines object boundaries within images and basically it is an image segmentation technique. The edges and corners in images can be found by detecting changes of image brightness or discontinuities sharply (Kizilkaya, 2008).

Segmentation can be classified as follows:

- Region Based
- Edge Based
- Pixel Based
- Feature Based Clustering
- Model Based

Edge detection techniques are done through detecting the maximum value of the first derivative or zero crossing of the second derivative. The representative first order differential operators (Roberts, Prewitt, Sobel, etc.) and second order differential operators (Laplace, LOG, etc.) (Rong et al., 2014). In (Biswas and Sil, 2012; Kabade and Sangam, 2016), the three main principles of the canny edge detection are as follows: low error rate, good localization of edge points and one response to a single edge.

Evaluation of the images showed that under noisy conditions, Canny, LoG, Sobel, Prewitt, Roberts's exhibit better performance, respectively (Maini and Aggarwa, 2009). In (Yuksel and Borlu, 2009), the Canny's edge detector was used to find the best region growing method for medical image segmentation (Biswas and Sil, 2012). Canny edge detection algorithm is used in this study.

The flowchart of the proposed method is shown in Figure 1.

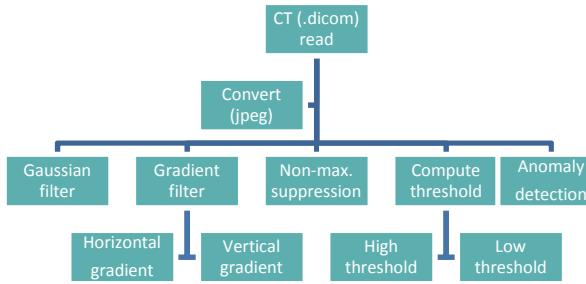


Figure.1 Canny edge detection flowchart

Algorithm:

1. Convolve with gradient filters (at multiple scales);

$$\vec{R}(i) \equiv (R_x(i), R_y(i)) = \nabla G(i; \sigma^2) * I(i) \quad (1)$$

2. Compute response magnitude;

$$S(i) = \sqrt{(R_x^2(i) + R_y^2(i))} \quad (2)$$

3. Compute local edge orientation (represented by unit normal):

$$\vec{X} = \begin{cases} (R_x(i), R_y(i)) / S(i), & \text{if } S(i) > \text{threshold} \\ \mathbf{0}, & \text{otherwise} \end{cases} \quad (3)$$

4. Peak detection (non-maximum suppression along edge normal).

5. Non-maximum suppression through scale, and hysteresis thresholding along edges (Jepson and Fleet, 2009). You can see (Canny, 1986) for algorithm details.

In the presented study, canny edge detector has been used to obtain anomaly segments and their boundaries.

The bone anomaly can be divided into two groups, namely primary and secondary (metastatic) tumors (Rice et al., 2014) and they are rarely encountered (Foo and Raby, 2005; Bakotic and Huvos, 2001). The general classification of bone tumors is given by (Ozer et al., 2014) as below :

- Benign bone tumors
- Benign/aggressive bone tumors
- Malignant bone tumor.

3. METHODS

Computed Tomography images are obtained from Faculty of Medicine, Bezmialem Vakif University. Digital medical image format is DICOM (Digital Imaging and Communications in Medicine). CT images of ten male patient's foot (245 slices and 50 test data) are used. CT image stack is given in Figure 2.

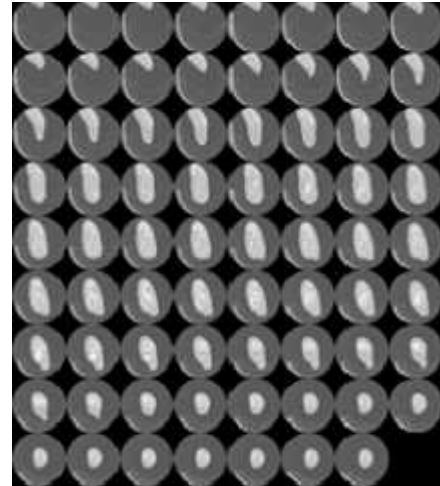


Figure.2 CT Images stack

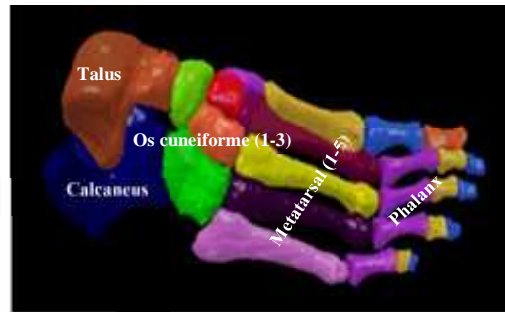


Figure.3 3D Foot anatomy

The used parameters are detector collimation of 64x2mm, scanning thickness of 1-5mm, pixel sizes of 512x512 in radiometric resolution of 16 bits' gray levels. The axial images in Digital Imaging and Communications in Medicine format were first transferred into a personal computer.

Proposed Algorithm;

- Step 1: CT (.dicom) image read
- Step 2: Calculating the horizontal & vertical gradient
- Step 3: Determining gradient magnitude and gradient direction
- Step 4: Applying non-maximal suppression
- Step 5: Computing high and low thresholds
- Step 6: Hysteresis thresholding
- Step 7: Output

Figure 4 shows (a) the CT .jpeg image and (b) 3D of foot in the window.



Figure. 4 CT .jpeg image and 3D model

Figure 5 shows the CT raw data in the window, the edge detection results of the canny in the slice has been

given in Figure 6.

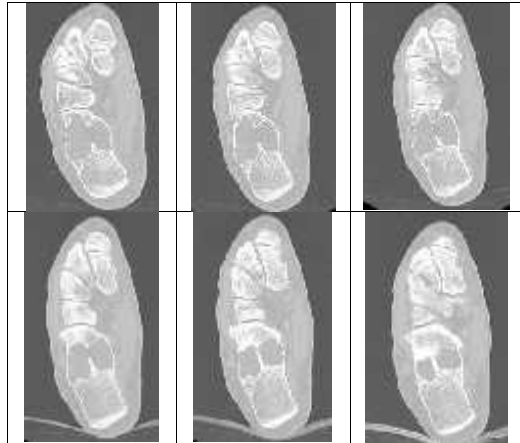


Figure.5 Original CT raw data

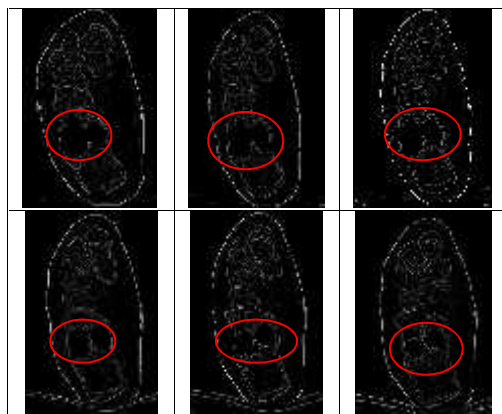


Figure.6 Examples of segmentation results by the proposed segmentation algorithm (Close-ups of the improved canny segmentation results (red))

A flowchart of the proposed method is shown in Fig. 6 and Fig.7. Original CT image and anomaly-background. The red frame indicates the anomaly, respectively. If there are two or more closed areas, there is anomaly in that bone.

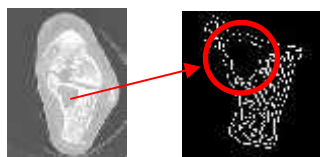


Figure.7 The flowchart of the proposed method

Matlab is used for image processing and detecting anomaly. In this study, detecting the anomaly and segmentation of the tumor and tumor-like lesion have been performed. Canny edge detection algorithm has good performance for edge detection, localization and only one response to a single edge.

In this study used receiver operating characteristic curve (ROC) for accuracy analysis. The measure of accuracy is the area under the ROC curve, often used as “AUC” for area under curve. The AUC is global a summary measure (Obuchowski, 2005). The method obtains satisfactory performances in terms of accuracy

and F-measure the ROC.

$$\text{Accuracy} = \frac{\text{TP} + \text{TN}}{\text{TP} + \text{TN} + \text{FP} + \text{FN}} \quad (4)$$

$$\text{F - Measure} = \frac{2\text{TP}}{2\text{TP} + \text{TN} + \text{FN}} \quad (5)$$

where; TP is the number of true positives, TN is the number of true negatives, FP is the number of false positives and FN is the number of false negatives.

To verify the proposed classification method, a comparison experiment with different two of test samples is performed. 50 different of image samples are selected for testing in this experiment and divided into two: anomaly and normal. After these process, 245 images were processed in the algorithm in order. The images are divided into anomaly or not. After this, roc analysis was done.

4. RESULTS AND CONCLUSION

This study proposes edge-based segmentation method for automatic bone of foot anomaly segmentation on CT images. An accuracy of 0.86 and F-measure of 0.92 are obtained, respectively. Since edge detection is an important step in digital image processing, it is necessary to point out the true edges to get the best results from the image process. So it is important to choose edge detector that suitable best to the application. Canny edge detector method enables users segment anomaly in MDCT of foot too quickly and efficiently. Canny edge detection algorithm is one of the best algorithms since it provides more accurate edge detection values for applying searching algorithm in the this work (Biswas and Sil, 2012; Catal Reis et al, 2016). In this work, canny edge detection algorithm for extracting the edge for the medical images have been used. We are also planning a further similar study on different bones' tumor.

REFERENCES

- Bakotic, B. and Huvos, A.G., 2001. Tumors of the Bones of the Feet: The Clinicopathologic Features of 150 Cases, *Journal of Foot & Ankle Surgery*, 40(5), pp. 277 -286.
- Biswas, R. and Sil, J., 2012. An Improved Canny Edge Detection Algorithm Based on Type-2 Fuzzy Sets, *Procedia Technology*, 4, pp. 820 – 824.
- Canny, J.F., 1983. Finding Edges and Lines in Images, Technical Report AI-TR-720, MIT, Artificial Intelligence Laboratory, Cambridge, MA.
- Canny, J.F., 1986. A Computational Approach to Edge Detection, *IEEE Transactions on Pattern Analysis and Machine Intelligence*, 8(6), pp. 679-698.
- Catal Reis, H., Bayram, B. and Seker, D.Z., 2016. Bone Tumor Segmentation by Gradient Operators from CT Images, *Selcuk International Scientific Conference on Applied Sciences (The Selçuk ISCAS 2016)*, 27-30 September, Antalya, Turkey.

- Doi, K., 2007. Computer-Aided Diagnosis in Medical Imaging: Historical Review, Current Status and Future Potential, *Comput Med Imaging Graph.*, 31(4-5), pp. 198–211.
- Foo, L.F. and Raby, N., 2005. Tumors and Tumor-like Lesions in the Foot and Ankle, *Clinical Radiology*, 60, pp. 308–332.
- Giger, M.L., Huo, Z., Kupinski, M.A., Vyborny, C.J., 2000. Computer-Aided Diagnosis in Mammography. In: Fitzpatrick JM, Sonka M, editors. *The Handbook of Medical Imaging*, volume 2 *Medical Imaging Processing and Analysis*, SPIE, pp. 915–1004.
- Gonzalez, R.C. and Woods, R.E., 2007. *Digital Image Processing*, 2nd ed., Beijing: Publishing House of Electronics Industry.
- Hasbek Z., Salk I., Yucel B., Akgul Babacan, N., 2013. Which Imaging Method to Choose for Detection of Bone Metastases? *Bone Scintigraphy, CT, 18F-FDG PET/CT or MR?* *Bozok Med J*, 3(3), pp. 44-50.
- Jepson, A.D. and Fleet, D.J., *Edge Detection*, 2009, <http://www.cs.toronto.edu/~jepson/csc2503/edgeDetection.pdf>, 1 Nov 2015.
- Kabade, A.L. and Sangam, V.G., 2016. Canny Edge Detection Algorithm, *International Journal of Advanced Research in Electronics and Communication Engineering (IJARECE)*, 5(5), pp. 1292-1296.
- Kizilkaya, A., 2008. Department of Electrical Engineering, Lecture Note, Pamukkale University, Denizli- Turkey.
- Lodwick, G.S., Haun, C.L., Smith, W.E., Keller, R.F. and Robertson, E.D., 1963. Computer Diagnosis of Primary Bone Tumors. A prelim. Report, 80, pp. 273-5.
- Maini, R. and Aggarwa, H., 2009. Study and Comparison of Various Image Edge Detection Techniques, *International Journal of Image Processing (IJIP)*, 3(1), pp. 1-11.
- Mascard, E., Gaspar, N., Brugières, L., Glorion, C., Pannier, S. and Gomez-Brouchet, A., 2017. Malignant Tumours of the Foot and Ankle, *EFORT Open Rev.*, 2(5), pp. 261–271.
- Obuchowski, N.A., 2005. ROC Analysis, *Fundamentals of Clinical Research for Radiologists*, American College of Radiology (ACR), 184, pp. 364-372.
- Ozer, D., Er, T., Aycan O.E., Oke, R., Coskun, M. and Kabukcuoglu, Y.S., 2014. May Bone Cement Be Used To Treat Benign Aggressive Bone Tumors of the Feet with Confidence? *The Foot*, 24, pp. 1–5.
- Rice, B.M., Todd, N.W., Jensen, R., Rush, S.M. and William Rogers, W., 2014. Metastatic Calcaneal Lesion Associated with Uterine Carcinosarcoma, *The Journal of Foot & Ankle Surgery*, 53, pp. 364–368.
- Rong, W., Li, Z., Zhang, W. and Sun, L., 2014. An Improved Canny Edge Detection Algorithm, *Mechatronics and Automation (ICMA)*, IEEE International Conference, 3-6 Aug. 2014, Tianjin, China.
- Toriwaki, J., Suenaga, Y., Negoro, T, et al., 1973. Pattern Recognition of Chest X-Ray Images, *Computer Graphics and Image Processing*, 2, pp. 252–271.
- Yogamangalam, R. and Karthikeyan, B., 2013. Segmentation Techniques Comparison in Image Processing, *International Journal of Engineering and Technology (IJET)*, 5(1) (Feb-Mar).



*International Journal of Engineering and Geosciences (IJEG),
Vol; 3; , Issue; 1, pp. 006-011, February, 2018, ISSN 2548-0960, Turkey
DOI: [10.26833/ijeg.328919](https://doi.org/10.26833/ijeg.328919)*

PHOTOGRAMMETRIC MODELLING OF HASBEY DAR'ÜLHUFFAZ (MASJID) USING AN UNMANNED AERIAL VEHICLE

asi, A.,^{1*} Yakar M.,²

¹ Selçuk University, Faculty of Engineering, Department of Geomatics Engineering, Konya, Turkey
(sasihmet@gmail.com)

² Mersin University, Faculty of Engineering, Department of Geomatics Engineering, Mersin, Turkey
(myakar@mersin.edu.tr)

ORCID 0000-0002-1217-3887; ORCID 0000-0002-2664-6251

*Corresponding Author, Received:17/07/2017, Accepted: 06/09/2017

ABSTRACT: Cultural assets constitute the bridge between our past and future in the geography we live. Protecting the artifacts that survived until today and bear the experiences of history and, more importantly, passing these down to future generations are of great importance for our country. Protecting and sustaining cultural assets are duties of mankind for the sake of ownership of universal values. Therefore, documenting all cultural assets in the geography we live in is a necessity. To this end, documentation practices for cultural assets bear great significance in terms of both historical development and contributing to the world cultural heritage.

This article discusses the 3D photogrammetric modelling of Hasbey Dar'ülhuffaz (madrasa for training hafiz) from the Karamanids era, which is located in Ayine Street, Mücellit Neighborhood, Meram District in Konya Province. Within this scope, firstly, four control points that cover the aforementioned cultural asset were established in the study. The coordinates for these points were determined with a Topcon FC-250 GPS. Then, photographs of the cultural asset were captured with Nikon D90 camera and aerial photographs were taken with DJI Phantom 4 unmanned aerial vehicle. DJI Go 4 and Pix4Dcapture mobile applications were used to capture photographs using the unmanned aerial vehicle. All data obtained were evaluated via Agisoft PhotoScan and Netcad software, and a 3D model of the artifact was acquired.

Documentation of the 3D models for artifacts in question contribute greatly to the world cultural heritage. At the same time, the 3D model obtained constitutes a substantial and accurate resource to pass down the artifacts to future generations. The most important point is to provide an opportunity for a faithful restoration in case of any potential damage to this historical artifact from physical intervention and natural disasters. It is foreseen that this model will also offer solutions to the problems of many professional disciplines today.

Keywords: *Unmanned Aerial Vehicle, 3D Modelling, Photogrammetry, Historical Artifact, Cultural Heritage*

1. INTRODUCTION

Historical artifacts that stand as cultural heritage are buildings that connect the past and future of the world. The geography we live in has been home to various cultures and civilizations. Societies belonging to these cultures and civilizations built many assets that reflect their lives and experiences. Thus, it is our duty to display ownership for the cultural assets in our country and sustain them for the sake of history and as a sign of our fidelity. Documentation of cultural assets bearing historical value in our country carries great significance in that the documentation practice helps protect and sustain these structures (Yakar et al., 2011).

The said structures are at risk of being destroyed by natural or unnatural physical interventions at any moment. To this date, countries having cultural and natural heritage have fallen short of protecting such heritage due to a lack of economic, scientific and technical resources. Therefore, it is a national duty of humanity to share scientific studies and recent techniques for the protection of such cultural heritage (Yakar et al., 2009).

Artifacts that stand as cultural assets have detailed and elaborative architectures. For this reason, digital photogrammetry technique is used for the documentation of such cultural assets. Digital photogrammetry technique provides us with the fastest, safest and most accurate data. This technique also employs the state-of-the-art measuring instruments and imaging systems the technology offers us.

In this study, both aerial photogrammetry and terrestrial photogrammetry techniques were used. Four control points that cover the periphery of the cultural asset to be modelled 3D were established in the study. Field coordinates of these points were measured with a GPS. Photographs of the cultural asset were captured using an unmanned aerial vehicle and a camera. Aerial photographs and terrestrial photographs were linked together through tie points.

The 3D model can be used by many professional disciplines. It can be a resource for the historical artifact in order to come up with solutions to problems that may occur in the future. Moreover, thanks to the technological devices used in aerial photogrammetry, the technique of this study establishes a link between history and technology.

2. PROTECTION AND DOCUMENTATION OF CULTURAL ASSETS

Documentation procedures for cultural assets having historical property in our country is of great importance. Artifacts can be restored thanks to these documentation procedures in the aftermath of possible damages due to natural disasters (Hanke et al., 2002). Meanwhile, these models can give people an idea in the future, should there be a need for sustaining the original structure of the artifact. They give future generations the correct information regarding the introduction of the past

societies (Uysal et al., 2013).

The 3D models obtained via photogrammetry technique constitute an accurate point of reference for administrators of the city and the country alike, facilitating their decision-making process.

3. FIELD OF STUDY

3.1 Hasbey Dar'ülhuffaz

The name of the cultural asset to be modelled 3D is Hasbey Dar'ülhuffaz (Masjid). It is located in No: 2 Ayine Street, Mücellit Neighborhood, Meram District in Konya Province. The coordinates of Hasbey Dar'ülhuffaz, a cultural asset, are 37°52'90.46" N latitude and 32°29'42.42" E longitude. It was built in 1421 A.D. during the Karamanids era by Mehmet, the son of Hodja Hasbey, as a madrasa for the hafiz. The artifact was registered by Konya Regional Board of Cultural Heritage Protection on November 13, 1982 (Gümü et al., 2010).

The artifact is made up of bricks and stones. Above the entrance door hangs an inscription with two lines. The west facade of the structure, which has a square layout, is intensely decorated. The drum of the masjid is covered with a dome which is rather high and made of brick. The mihrab is decorated with mosaic tile pieces some parts of which have not survived until today. Moreover, the artifact has an underground tomb (Gümü et al., 2010).



Figure 1. Location and general appearance of Hasbey Dar'ülhuffaz

3.2 Technical Equipment and Software Used in the Study

For the 3D modelling of the cultural asset, after establishing four ground control points to cover the periphery of the said asset, coordinates of these points were determined with Topcon FC-250 GPS. A Nikon D90 camera and a DJI Phantom 4 unmanned aerial vehicle were used to take photographs of the historical artifact. For flying the unmanned aerial vehicle, the DJI

Go 4 mobile application was utilized. Furthermore, weather conditions were monitored via UAV Forecast mobile application to ensure favorable weather conditions were present for flight.



Figure 2. Nikon D90 camera, Topcon FC-250 GPS and DJI Phantom 4 unmanned aerial vehicle

Field coordinates of the ground control points were assessed with Netcad software. Agisoft PhotoScan software was used for the photogrammetric evaluation of the photographs taken.

3.3 Photogrammetric Evaluation

The 3D model of the artifact was obtained from the documentation processes for the cultural asset.

In this study, we established four ground control points around the artifact. The field coordinates of these ground control points were measured with Topcon FC-250 GPS. Aerial and terrestrial photographs of the artifact were captured using an unmanned aerial vehicle and a camera.

The 3D modelling of Hasbey Dar'ülhuffaz via the photogrammetry technique was carried out in two stages, namely field survey and desktop work. In field surveys, four ground control points were established around the artifact. The coordinates of these points were determined via GPS. The IMU and Compass calibrations for the DJI Phantom 4, the unmanned aerial vehicle, were performed prior to capturing photographs of the artifact. Then, terrestrial and aerial photographs of the artifact were taken with the unmanned aerial vehicle and camera. Since the unmanned aerial vehicle used in this study contains a compass, a GPS and two IMUs, the photographs captured with it include latitude, longitude and altitude information. The model which was built by converting coordinates for ground control points established for the field was created with coordinates.

The software used in the evaluation of the photographs of the artifact creates a calibration report of the cameras used. Error corrections are included in the calculation. In order to integrate terrestrial photographs

captured with camera and aerial photographs captured with unmanned aerial vehicle, tie points were placed in sharp details among photos. These points were aligned and matched on details that correspond to other photographs. After alignment and matching, the 3D model of the artifact was built via photogrammetric software using all the data obtained from field surveys and desktop work.

3.3.1 Field Survey for Hasbey Dar'ülhuffaz

In our country, unmanned aerial vehicles over a certain weight limit must be registered within the system of the Directorate General of Civil Aviation. The unmanned aerial vehicle used in the study was registered before the Directorate General of Civil Aviation. Then, a flight permit was obtained from Konya Governor's Office, and the district police department was provided with information on the location and time of the flight. All these processes are extremely important in terms of public safety as well as flight safety. After the flight permit was obtained and relevant departments were notified, conditions for a safe flight were ensured.

Four control points were established around the artifact to be modelled after the necessary flight permits were obtained. While establishing these points, attention was paid so that points saw one another and nothing obscured the aerial photographs.



Figure 3. Establishing ground control points

Four control points were established around the artifact to be modelled. Coordinates for these points were determined with Topcon FC-250 GPS and ITRF96 (Epok: 2005). Moreover, the base map of the artifact was taken from the field and vector drawing of it was made via Netcad software.



Figure 4. The base map drawing for the artifact

The UAV Forecast application was used to determine whether the flight zone was fit to fly the unmanned aerial vehicle. This application utilized the information regarding sunrise and sunset time, the speed and direction of the wind, if available, whether the weather is overcast as well as sight distance to determine whether it was a day fit to fly, which it was.



Figure 5. Checking weather conditions for flight

After making sure that the weather conditions were fit for flight, the DJI Phantom 4 and DJI Go 4 mobile application were integrated. Then, the compass of the unmanned aerial vehicle was calibrated. This calibration is important as it eliminates certain system errors that occur while the unmanned aerial vehicle is capturing photographs. The key aspect of the calibration is that while taking photographs, it can ensure the unmanned aerial vehicle vertically suspends in the air in a stable manner.

The Compass is calibrated by rotating the unmanned aerial vehicle 360° around its own axis both horizontally and vertically.

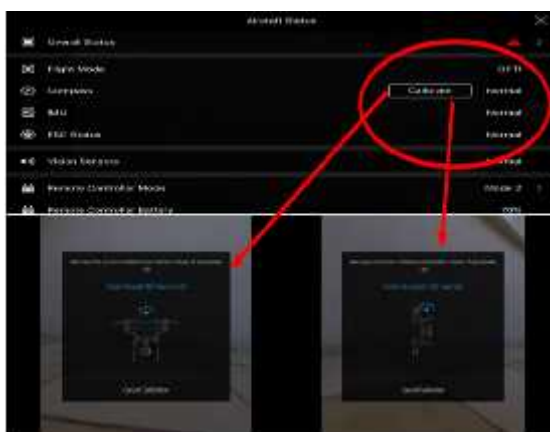


Figure 6. Calibrating the compass of the unmanned aerial vehicle

The compass calibration was followed by the calibration of the IMU. The IMU helps stabilize the unmanned aerial vehicle especially in windy weather conditions

and eliminates drift errors in photographs. The calibration process took approximately five minutes.



Figure 7. Calibrating the IMU of the unmanned aerial vehicle

Photographs of Hasbey Dar'ülhuffaz were manually controlled by the unmanned aerial vehicle. Each facade of the cultural heritage was photographed, ensuring a high overlapping rate. Aerial photographs were supported by terrestrial photographs taken with the Nikon D90 camera.

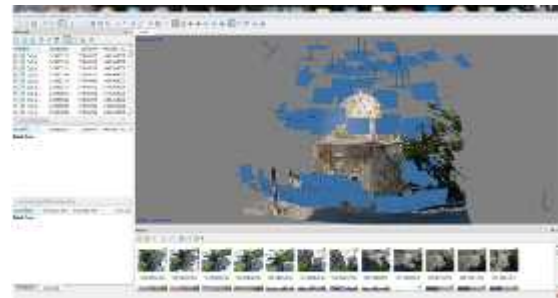


Figure 8. Overlapping photographs of the artifact

The accuracy of geographical coordinates of the cultural asset photographs which were taken by the unmanned aerial vehicle was checked via Google Earth.

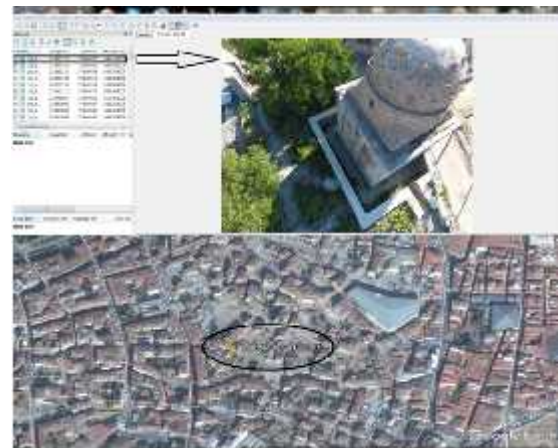


Figure 9. Consistency of photograph and satellite coordinates

Field surveys for Hasbey Dar'ülhuffaz were thus completed. The next stage involved the desktop work.

3.3.2 Desktop Work for Hasbey Dar'ülhuffaz

Photographs of Hasbey Dar'ülhuffaz were evaluated via Agisoft PhotoScan software. First, the photographs were aligned with a high overlapping rate and organized in a certain order. As a result of the alignment, 26,638 point clouds were generated. The process took 4 hours and 22 minutes.

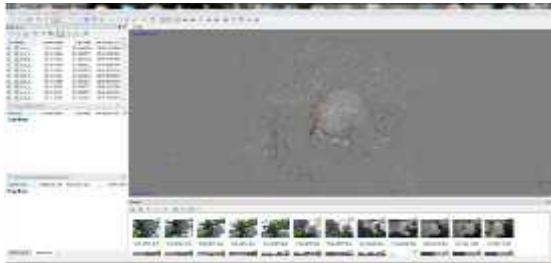


Figure 10. Alignment of Hasbey Dar'ülhuffaz photographs

The aligned photographs helped acquire a point cloud via the high overlapping rate. The second step was to build a dense point cloud. Workflow - Build Dense Cloud - High - Mild option sequence was followed. This process took 7 hours and 23 minutes. As a result, 16,261,059 point clouds were generated.

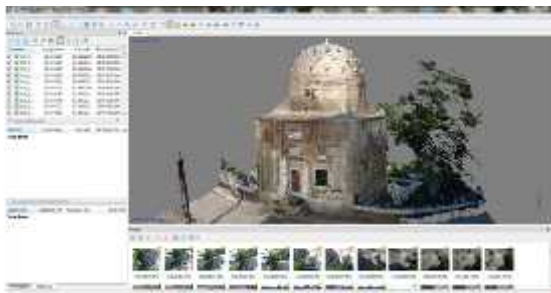


Figure 11. Building a dense cloud for Hasbey Dar'ülhuffaz

Following the completion of building the dense cloud, Workflow - Build Mesh option sequence was followed in order to create a solid model of the dense cloud. Generally, in building modelling, Arbitrary - Dense Cloud - High option sequence was followed and a solid model was obtained by choosing the Enabled option under the Interpolation tab.



Figure 12. Creating a solid model from point cloud in Build Mesh option

Following the Build Mesh process, Workflow - Build Texture option sequence enabled texture building. In this study, Adaptive Orthophoto (used for vertical texture building) - Mosaic and Enable Color Correction options were used. Following the process, texture building for the solid model was completed.

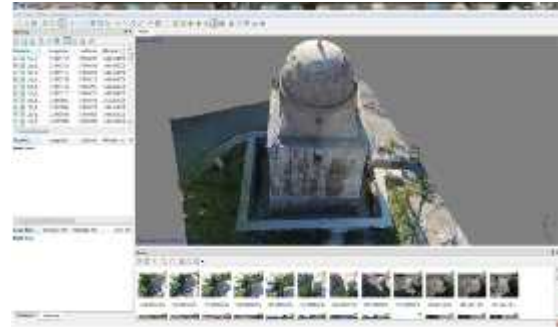


Figure 13. Texture building for the solid model

In order to obtain a high-quality look for the details and the meshes of the object, the Build Tiled Model option was chosen from the Workflow menu. The 3D model of Hasbey Dar'ülhuffaz then included coordinates.



Figure 14. General view of the 3D model (Build Tiled Model)

4. RESULTS

As a result of this study, a 3D model of Hasbey Dar'ülhuffaz that is located in Mücellit Neighborhood, Meram District in Konya Province was created via the photogrammetry technique. The 3D model of the artifact was built in two stages, namely field surveys and desktop work. During field surveys, ground control points were established, the coordinates of these points were determined via GPS and the overlapping photographs of the artifact were captured using an unmanned aerial vehicle and a camera. Then, all data obtained from the field were used to build a 3D model during desktop work. Coordinates on the ITRF-96 coordinate system are obtained from the field with a Topcon Fc-250 GPS. The accuracy of the coordinates obtained with the Gps varies between ± 2 cm and ± 4 cm.

The 3D model contributed to both the documentation processes for cultural assets of our country and the world cultural heritage. It provides a resource for faithful restoration of the artifact in case of any damage or destruction due to possible natural

disasters or physical interventions.

The aim of this study is that it constitutes a resource for solving the potential problems of many professional disciplines that may occur around the region in the future.

ACKNOWLEDGEMENTS

I would like to thank Prof. Murat YAKAR, my advisor, for sharing his knowledge and experience with me and for encouraging me to be a part of and contribute to documentation studies for cultural assets.

REFERENCES

- Gümü , H., Koçak, F., 2010. Inventory of Immovable Cultural and Natural Heritage of Konya Province. Konya Metropolitan Municipality, Archive for Immovables.
- Hanke, K., Grussenmeyer, P., Strelein, A., 2002. Digital Photogrammetry, Taylor & Francis, 300 – 301.
- Uysal, M., Toprak, A. S., Polat, N., 2013. ‘Three Dimensional Modeling of Afyon Gedik Ahmet Pasha (Imaret) Mosque by Photogrammetric Method’ Turkish National Photogrammetry and Remote Sensing Association Symposium, Trabzon
- Yakar, M., Yılmaz, H.M., Yıldız, F., Zeybek, M., entürk, H., Çelik, H., 2009. 3-Dimensional Modeling Study and Animation of Roman Period Works in Silifke-Mersin Region, TMMOB Chamber of Surveyors and Cadastre Engineers 12. Turkey Map Scientific and Technical Convention, Ankara.
- Yakar, M., Yıldız, F., Zeybek, M., Kocaman, E., Yolcu, M., Filiz, T., 2011. Photogrammetric Modeling of Monuments Eflatunpınar, FIG Working Week 2011 Bridging the Gap between Cultures, Marrakechk, Morocco
- Web Map Tile Service, www.agisoft.com [Accessed 25 Jun 2017].
- Web Map Tile Service, www.dji.com [Accessed 25 Jun 2017].
- Web Map Tile Service, <https://pix4d.com/> [Accessed 25 Jun 2017].
- Web Map Tile Service, <https://netcad.com.tr> [Accessed 30 Jun 2017].



*International Journal of Engineering and Geosciences (IJEG),
Vol: 3; , Issue;1, pp. 012-019, February, 2018, ISSN 2548-0960, Turkey,
DOI: [10.26833/ijeg.337806](https://doi.org/10.26833/ijeg.337806)*

COMPARISON OF GPS SATELLITE COORDINATES COMPUTED FROM BROADCAST AND IGS FINAL EPHEMERIDES

Tusat, E., ^{1*} Ozyuksel, F.,²

¹Selçuk University, Cumra School Of Applied Sciences, Department of Department of management Information Systems,
Cumra, Konya, Turkey (etusat@selcuk.edu.tr)

² Selcuk University, Engineering Faculty, Department of Geomatic Engineering, Konya, Turkey
(fethiozyuksel@gmail.com)

ORCID ID 0000-0003-4130-3764; ORCID ID 0000-0002-6868-8396

*Corresponding Author, Received: 12/09/2017, Accepted: 07/11/2017

ABSTRACT: There are mainly two different orbital information, namely broadcast ephemerides and IGS final ephemerides (IGS rapid, ultra rapid, predicted and final ephemerides) used in the GPS positioning. The broadcast ephemerides used in practice and real time are obtained through assessments derived from the observations from the USA GPS reference stations. Broadcast ephemerides are formed (depending on GPS week) from satellite information and the accuracies they provide are adequate in many GPS applications. On the other hand, several parameters (for example, information about gravity area, improved satellite orbit information, etc.) need to be known in order to attain high accuracy in engineering and geodetic applications. Final ephemeris information can be downloaded from the related web sites via the internet. In this study, Keplerian motion and Keplerian orbital parameters will be explained briefly and extensive information about ephemerides and numerical applications will be given. Within this scope, for GPS satellites, ECEF coordinates of the satellites were computed using the broadcast ephemerides. The coordinates computed by using broadcast ephemerides were compared with the coordinates obtained from the IGS final orbits.

Keywords: *GPS, Broadcast Ephemerides, IGS Ephemerides, Keplerian Orbital Parameters*

1. INTRODUCTION

Knowledge of ephemerides is an important issue for all GNSS applications because all ground positioning applications begin with the positions of GNSS satellites (Yoon, 2015). The computation and prediction of precise satellite orbits, together with appropriate observations and adjustment techniques is, for example, essential for the determination of;

- geocentric coordinates of observation stations,
- field parameters for the description of the terrestrial gravity field as well as for the determination of a precise and high resolution geoid,
- trajectories of land-, sea-, air-, and space-vehicles in real-time navigation,
- Earth's orientation parameters in space (Seeber, 1993)

Keplerian elements forming the fundamental information of the satellite orbit motion need to be known in order to make accurate orbit definitions in navigation and other relevant fields where satellite methods are used to determine positions. Satellite motions are expressed through Kepler's Laws and are defined via six Keplerian orbital elements (Seeber 1993, Hoffmann-Wellenhof et al. 1994, Warren 2002). These are shown in Figure 1 and explained in Table 1.

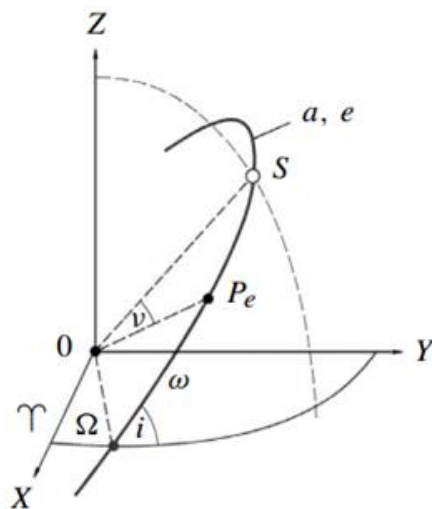


Figure 1 : Keplerian Orbital Elements (Seeber, 1993)

Three of the Keplerian orbital elements (a, e, P) describe the shape of the orbit while the other three elements (i, Ω, ω) enable orientation of the orbit in the ECEF (Earth Centered Earth Fixed) coordinate system.

Ephemerides data involving satellite orbital information are used to determine the position of a point on earth. Ephemerides data express Keplerian Orbital Information and data belonging to the momentary position of the satellite. Basis vector measured via GPS and point position accuracies vary depending on the accuracy of the ephemerides used in calculation.

Table 1 : Keplerian Orbital Elements (Warren, 2002)

Parameter	Explanation
Ω	Right ascension of ascending node (measured as radian on the equatorial plane)
i	Inclination of the Orbital Plane
ω	Argument of Perigee
a	Semi major axis of orbital plane (meter)
e	Numerical eccentricity of ellipse; $e \leq 0.01$
P	Epoch of Perigee Passage

2. GPS EPHEMERIDES

Ephemerides in practical usage are broadcast ephemerides that constitute the control unit of GPS and are obtained through observations. Although broadcast ephemerides provide adequate accuracy in many applications, they may not be adequate for applications requiring high accuracy. Broadcast ephemerides are delivered to users as navigation messages (Seeber, 1993).

The error that occurs when the accuracy of the satellite position information broadcast in GPS Navigation message is low or when it is broadcast deliberately erroneously is called ephemeris error. This error is one of the disturbing effects that are hard to model. Therefore, it is important to take these disturbing effects, which are defined as ephemeris error, into consideration in computation of satellite orbits and this depends on proper measurement and modeling of forces affecting satellites (Tusat and Turgut, 2003). Since ephemeris error is a result of prediction of satellite positions, the size of this error will increase as one moves away from the reference epoch for ephemerides. When the matter is analyzed in terms of the user, the error that will be caused by satellite error in Δr size in fundamental components (Δb) of base in b length can be expressed in the following equation (Kahveci and Yildiz, 2001).

$$\frac{\Delta b (m)}{b (km)} = \frac{\Delta r}{\rho_R^{SV} (km)} \quad (1)$$

Here, ρ_R^{SV} denotes the satellite-receiver distance. Thus, if satellite-receiver distance is taken to be approximately 20200 km, errors in lengths that will be obtained for different ephemeris errors and base lengths on the basis of equation (1) are shown in Table 2 (Kahveci and Yildiz, 2001).

Table 2: Error Rates in Baseline from Ephemeris Errors

Ephemeris Error (m)	Baseline (km)	Error (ppm)	Error (mm)
2.5	1	--	--
2.5	10	0.1	1
2.5	100	0.1	12
2.5	1000	0.1	124
0.05	1	--	--

0.05	10	--	--
0.05	100	0.002	0.2
0.05	1000	0.002	2.5

The effect of ephemeris error is quite low for baselines of a few kilometers. However, the size of this error increases significantly in cases where baselines reach a few kilometers, which causes a problem in the use of GPS system in geodetic applications that require a high level of accuracy (Kahveci and Yildiz, 2001). Main causes of the error in question involve atmospheric drag and pressure by solar radiation. Sizes of predicted orbit and real orbit may exhibit differences especially during periods of high solar activity. Accuracy of geocentric coordinates obtained through broadcast ephemerides is not better than $\pm 2\text{-}5$ cm (Seeber, 1993).

2.1 Broadcast Ephemerides

Users need to know real time satellite positions and satellite system time in order to perform navigation tasks. Orbital information included in the data signal is broadcast via navigation message. Navigation message is determined by the Control Unit and transmitted to users by GPS satellites as “broadcast”. The GPS navigation message file which contains the broadcast ephemeris gives the Keplerian parameters needed to compute the coordinates and clock correction for each satellite (Bidikar et al. 2014).

Broadcast ephemerides are used to compute the following items (Parkinson, 1996);

- satellite position at epoch,
- satellite velocity at epoch,
- three clock parameters per satellite,
- solar radiation pressure coefficients per satellite,
- y-axis acceleration bias,
- two clock parameters per monitor station, and
- one tropospheric scale factor per monitor station.

In the Kalman Filter process, predicted satellite positions are in the form of perturbation parameters and Keplerian elements (Figure 2). All parameters defining the satellite orbit and the state of the satellite clock are summarized in Table 3 below.

The parameters refer to a given reference epoch, t_{0e} for the ephemeris and t_{0c} for the clock, and they are based on a four hours curve fit (ICD, 1993). Hence, the representation of the satellite trajectory is achieved through a sequence of different disturbed Keplerian orbits (Seeber 1993).

The parameter sets in Table 3 are used to compute satellite time and satellite coordinates. The first group of the parameters are used for real satellite time. The second group defines a Kepler ellipse in reference epoch while the third group includes nine perturbation parameters.

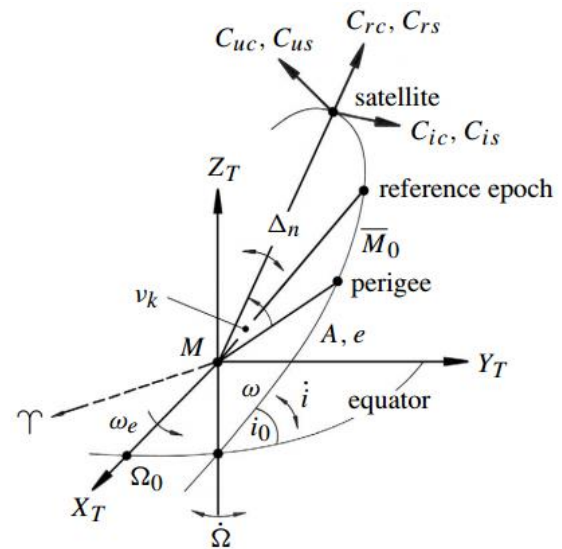


Figure 2 : Keplerian and perturbed parameters in broadcast ephemerides (Seeber, 1993)

Table 3 : Parameters of Broadcast Ephemerides (Seeber, 1993)

Time Parameters	
t_{0e}	Reference time, ephemerides parameters [s]
t_{0c}	Reference time, clock parameters [s]
a_0, a_1, a_2	Polynomial coefficients for clock corrections (bias [s], drift [s/s], drift rate [s/s ²])
<i>IODC</i>	Issue of Data, Clock, arbitrary identification number
Keplerian Parameters	
$\sqrt{a}, e, i_0, \Omega_0, \omega, M_0$	Keplerian elements of T_{0e}
<i>IODE</i>	Issue of Data, Ephemeris, arbitrary identification number
Perturbation Parameters	
Δn	Mean motion difference from computed value [semicircles/s]
di/dt (or <i>IDOT</i>)	Rate of change for inclination angle, (radian/second)
$\dot{\Omega}$	Rate of change in ascending node right ascension
C_{uc}, C_{us}	Correction coefficients for perigee argument, (radian)
C_{rc}, C_{rs}	Correction coefficients for geocentric distance, (meter)
C_{ic}, C_{is}	Correction coefficients for inclination angle, (radian)

2.2 IGS Final Ephemerides

Precise ephemerides and clock parameters depend on observations at monitor stations scattered across the world. Dual-frequency receivers that could measure both code phases and carrier phases of all visible satellites were established at some stations. Satellite errors can be purged of time errors of the station clock through use of

high precision oscillators (rubidium-cesium atomic standard) (Seeber, 1993). Data files are in general compatible with SP3 (standard product 3) data format (Remondi, 1991; Hilla, 2002; IGS 2017).

Today, the most important source for final ephemerides and other GPS products is IGS. Production of IGS (International GNSS Service) orbital information began with an experimental GPS measurement campaign that took place on 21st June 1992. (Kahveci and Yildiz, 2001) Unlike broadcast ephemerides, IGS orbits are formed from phase observations made in an intensive global network. Figure 3 shows IGS points in the world.



Figure 3 : IGS Network (IGS, 2017)

Today, IGS is responsible for collection, archiving and distribution of GPS measurements that could be used, with adequate accuracy, in scientific studies and engineering applications. These GPS measurements are used to obtain the following products (IGS, 2017).

- High accuracy GPS satellite ephemerides
- Earth rotation parameters (ERP)
- Coordinates of IGS monitor stations and their velocities
- Clock information belonging to GPS satellites and IGS monitor stations
- Computation of tropospheric zenith path delay

IGS products enable improvement and development of the ITRF system, determination of the movements of earth's crust, identification of changes on sea surface and provide high accuracy required by ionospheric studies. IGS performs these tasks within the following structure.

- A global observation network consisting of 506 stations
 - Three global data centers
 - o CDDIS (Crustal Dynamics Data Information System at Goddard Space Flight Center, USA)
 - o IGN (Institut Geographique National, France)
 - o SIO (Scripps Institution Oceanography)
 - Seven centers of analysis; CODE, NRCAN (EMR), ESA, JPL, GFZ, NGS and SIO.

The task of centers of analysis is to produce daily global data uninterruptedly (Kahveci and Yildiz, 2001). IGS produces four different pieces of orbital information according to orbits and clocks: IGS-Ultra-Speed, IGS Speedy, IGS Result orbital information (see Table 4).

Table 4 : IGS GPS satellite and clock accuracy (IGS, 2017)

Type	Accuracy		Latency	Updates	Sample Interval
	orbits				
Broadcast	orbits	~100 cm	real time	--	daily
	Sat. Clocks	~5 ns RMS ~2.5 ns Sdev			
Ultra-Rapid (predicted half)	orbits	~5 cm	real time	at 03, 09, 15, 21 UTC	15 min
	Sat. Clocks	~3 ns RMS ~1.5 ns Sdev			
Ultra-Rapid (observed half)	orbits	~3 cm	3 - 9 hours	at 03, 09, 15, 21 UTC	15 min
	Sat. Clocks	~150 ps RMS ~50 ps Sdev			
Rapid	orbits	~2.5 cm	17 - 41 hours	at 17 UTC daily	15 min
	Sat. & Stn. Clocks	~75 ps RMS ~25 ps Sdev			5 min
Final	orbits	~2.5 cm	12 - 18 days	every Thursday	15 min
	Sat. & Stn. Clocks	~75 ps RMS ~20 ps Sdev			Sat.: 30s Stn.: 5 min

3. MATERIAL AND METHOD

So far, GPS satellite orbits have been explained. In this regard, GPS satellite coordinates were computed in the ECEF coordinate system using the IGS final (igs18632.sp3) and broadcast ephemerides (brdc2650.15n) data belonging to September 22, 2015 at 12.00 hours in order to investigate the effect of ephemerides information on coordinates, and comparisons were made. In the numerical application conducted, the effect of broadcast ephemerides belonging to the points on satellite coordinates was investigated by changing only the orbital information from among the selected parameters in the comparison.

Computation of ECEF Coordinates from Satellite Orbits

RINEX (Receiver INdependent EXchange format) navigation file data are used to compute a GPS satellite orbit or its position at a certain moment in ECEF coordinate system. (Figure 4).

```

1 15 9 22 12 0 0.0
0.961590558250E-06 0.682121826330E-12 0.000000000000E+00 0.470000000000E+02 0.347187500000E+02
0.469659012742E-02 0.954605638981E-05 0.515366348839E+04 0.216000000000E+06 0.800937414169E-07
0.197343750000E+03 0.475413498332E+00 0.799747598412E-08 0.40001662300E-10 0.100000000000E+01
0.000000000000E+00 0.512227416039E-08 0.470000000000E+02 0.214380000000E+06 0.400000000000E+01
    
```

Figure 4 : RINEX data block for SV 1

Ephemerides parameters used in the computations are given Table 3. It is possible to compute highly accurate satellite coordinates in the ECEF coordinate

system using these data in a certain algorithm.

Satellite Position Computation Algorithm

Computation of the position of a satellite in ECEF coordinate system is quite simple. The algorithm to be used to this end is given in Table 5. E_k and V_k variables, which were not in linear correlation, were found using Newton-Raphson iteration technique.

Table 5 : Satellite Position Computation Algorithm

$GM_e = 3.986008 \times 10^4 \text{ m}^3/\text{s}^2$	Gravitational Constant
$\dot{\Omega}_e = 7.292115167 \times 10^{-5} \text{ rad/s}$	Earth rotation rate
$a = (\sqrt{a})^2$	Semi-major axis
$n_0 = \sqrt{\frac{GM}{a^3}}$	Computed mean motion
$n = n_0 + \Delta n$	Corrected mean motion
$t_k = t - t_{0e}$	Time according to t_{0e}
$M_k = M_0 + n \cdot t_k$	Mean anomaly
$E_k = M_k + e \cdot \sin E_k$	Eccentric anomaly
$V_k = \tan^{-1}\left(\frac{\sqrt{1-e^2} \cdot \sin E_k}{\cos E_k - e}\right)$	True anomaly
$V_{K'} = \cos^{-1}\left(\frac{e + \cos f_n}{1 + e \cos f_n}\right)$	True anomaly
$U_k = \omega + V_k$	Argument of latitude
$\delta U_k = C_{uc} \cdot \cos 2U_k + C_{us} \cdot \sin 2U_k$	Argument of latitude correction
$\delta r_k = C_{rc} \cdot \cos 2U_k + C_{rs} \cdot \sin 2U_k$	Radius correction
$\delta i_k = C_{ic} \cdot \cos 2U_k + C_{is} \cdot \sin 2U_k$	Inclination correction
$\Phi_k = U_k + \delta U_k$	Corrected argument of latitude
$r_k = a(1 - e \cdot \cos E_k) + \delta r_k$	Corrected radius
$i_k = i_0 + i \cdot t_k + \delta i_k$	Corrected inclination
$\Omega_k = \Omega_0 + (\dot{\Omega} - \dot{\Omega}_e)t_k - \dot{\Omega}_e t_{0e}$	Corrected longitude of ascending node
$X'_k = r_k \cdot \cos \Phi_k$	Position in the orbital plane
$Y'_k = r_k \cdot \sin \Phi_k$	
$X_k = X'_k \cdot \cos \Omega_k - Y'_k \cdot \sin \Omega_k \cdot \cos i_k$	Earth fixed geocentric satellite coordinates
$Y_k = X'_k \cdot \sin \Omega_k + Y'_k \cdot \cos \Omega_k \cdot \cos i_k$	
$Z_k = Y'_k \cdot \sin i_k$	

4. RESULTS AND DISCUSSION

For a comparison, the data obtained from a broadcast ephemeris file belonging to the selected time and all the coordinates in the ECEF system belonging to all the satellites were computed using the algorithm (see Table 5) and the results are given in Table 6. Since broadcast ephemerides information belonging to satellites 19 and 28 did not exist for the time we studied, it was not included in the computations and comparisons.

Table 6 : Coordinates Computed from Broadcast Ephemeris Data

BROADCAST EPHEMERIDES			
Date : 22.09.2015			
Time : 12 00 00.0 (UTC)			
SV	X (m)	Y (m)	Z (m)
PG01 / 1	13241509.1112	-22684517.4902	-3185779.0525
PG02 / 2	-19062942.1707	8040568.1264	-16021004.7228
PG03 / 3	10524879.3394	-13434155.3029	-20348279.9791
PG04 / 4	17487635.7595	-18899496.8878	5580890.8762
PG05 / 5	-25726352.4852	2709436.6092	6395764.0177
PG06 / 6	-15102048.5066	-4355823.4206	-21409473.3875
PG07 / 7	1496332.7481	-20904086.3120	16200889.5707
PG08 / 8	9613449.6557	-13567567.5895	20756256.7077
PG09 / 9	-6982217.0162	-24840578.1163	-6271115.2489
PG10 / 10	18020769.3446	3708296.6187	19272097.6589
PG11 / 11	10220819.5620	-23855161.8523	4866821.5666
PG12 / 12	-13429111.3494	11403133.8642	-19910724.6289
PG13 / 13	-14751728.3410	2703241.8466	21782990.8531
PG14 / 14	14467152.0676	20339524.5241	-9046264.9330
PG15 / 15	-9148103.2099	14508567.5799	20105616.2170
PG16 / 16	25972823.0282	-282111.9732	6335651.6228
PG17 / 17	-15209695.7659	-19577725.9601	-9512594.6810
PG18 / 18	9998746.5952	15467674.9555	19733909.5573
PG20 / 20	-13952448.9143	13459192.4687	18035077.8103
PG21 / 21	3030146.4229	19664885.4718	18152398.9758
PG22 / 22	21902903.8949	10072173.1631	11577960.4784
PG23 / 23	4016930.7221	-19851266.3489	-16786537.5994
PG24 / 24	-14556384.6682	22111328.9425	-224097.5724
PG25 / 25	1034402.1893	14955831.4442	-22033883.4358
PG26 / 26	25790651.8787	4884605.0664	-4080593.8351
PG27 / 27	15971808.8445	-394385.3141	21211096.3291
PG29 / 29	3925251.3408	24880784.6118	-8473995.8229
PG30 / 30	-7846485.3755	-14067794.7995	21104373.4715
PG31 / 31	15397134.8865	3526605.8571	-21275951.9003
PG32 / 32	21311233.5969	-6694899.2395	-13990519.1669

Satellite coordinates existing in current IGS final ephemerides file are given in Table 7.

Table 7 : Coordinates Taken from IGS Final Ephemerides File

SV	IGS FINAL EPHEMERIDES (PG)		
	22.09.2015 - 12 00 00.0 (UTC)		
	X (km)	Y (km)	Z (km)
PG01 / 1	13241.510267	-22684.518437	-3185.778312
PG02 / 2	-19062.942489	8040.569306	-16021.003732
PG03 / 3	10524.880813	-13434.156207	-20348.279989
PG04 / 4	17487.636021	-18899.497890	5580.890525
PG05 / 5	-25726.352210	2709.437346	6395.764498
PG06 / 6	-15102.049290	-4355.823474	-21409.474085
PG07 / 7	1496.332264	-20904.086346	16200.889743
PG08 / 8	9613.449439	-13567.568723	20756.257558
PG09 / 9	-6982.216570	-24840.579318	-6271.115865
PG10 / 10	18020.769915	3708.298193	19272.098083
PG11 / 11	10220.820960	-23855.162761	4866.822869
PG12 / 12	-13429.111902	11403.134108	-19910.723909
PG13 / 13	-14751.729370	2703.244991	21782.991689
PG14 / 14	14467.151791	20339.526524	-9046.265445
PG15 / 15	-9148.104842	14508.566576	20105.615974
PG16 / 16	25972.824222	-282.113556	6335.654492
PG17 / 17	-15209.694542	-19577.726766	-9512.594024
PG18 / 18	9998.748167	15467.676057	19733.910223
PG20 / 20	-13952.450041	13459.192872	18035.078960
PG21 / 21	3030.148062	19664.885926	18152.400788
PG22 / 22	21902.903891	10072.173885	11577.959609
PG23 / 23	4016.930809	-19851.266599	-16786.537380
PG24 / 24	-14556.385671	22111.329422	-224.097685
PG25 / 25	1034.402967	14955.832070	-22033.884220
PG26 / 26	25790.653160	4884.605494	-4080.593578
PG27 / 27	15971.809573	-394.384769	21211.097228
PG29 / 29	3925.250834	24880.784699	-8473.995905
PG30 / 30	-7846.486155	-14067.795260	21104.374161
PG31 / 31	15397.134642	3526.606158	-21275.951929
PG32 / 32	21311.233542	-6694.900451	-13990.520418

When the coordinates obtained from two different types of ephemerides information were compared, the differences in Table 8 were reached and they were shown in Figure 5.

Table 8 : Differences in Coordinates Obtained from Broadcast Ephemeris and IGS Final Ephemeris Data

SV	DIFFERENCES		
	ΔX (m)	ΔY (m)	ΔZ (m)
PG01 / 1	1.1558	-0.9468	0.7405
PG02 / 2	-0.3183	1.1796	0.9908
PG03 / 3	1.4736	-0.9041	-0.0099
PG04 / 4	0.2615	-1.0022	-0.3512
PG05 / 5	0.2752	0.7368	0.4803
PG06 / 6	-0.7834	-0.0534	-0.6975
PG07 / 7	-0.4841	-0.0340	0.1723
PG08 / 8	-0.2167	-1.1335	0.8503
PG09 / 9	0.4462	-1.2017	-0.6161
PG10 / 10	0.5704	1.5743	0.4241
PG11 / 11	1.3980	-0.9087	1.3024
PG12 / 12	-0.5526	0.2438	0.7199
PG13 / 13	-1.0290	3.1444	0.8359
PG14 / 14	-0.2766	1.9999	-0.5120
PG15 / 15	-1.6321	-1.0039	-0.2430
PG16 / 16	1.1938	-1.5828	2.8692
PG17 / 17	1.2239	-0.8059	0.6570
PG18 / 18	1.5718	1.1015	0.6657
PG20 / 20	-1.1267	0.4033	1.1497
PG21 / 21	1.6391	0.4542	1.8122
PG22 / 22	-0.0039	0.7219	-0.8694
PG23 / 23	0.0869	-0.2502	0.2194
PG24 / 24	-1.0028	0.4795	-0.1126
PG25 / 25	0.7777	0.6258	-0.7842
PG26 / 26	1.2813	0.4276	0.2571
PG27 / 27	0.7285	0.5451	0.8989
PG29 / 29	-0.5068	0.0872	-0.0821
PG30 / 30	-0.7795	-0.4605	0.6895
PG31 / 31	-0.2445	0.3009	-0.0287
PG32 / 32	-0.0549	-1.2115	-1.2511
Maximum	1.6391	3.1444	2.8692
Minimum	-1.6321	-1.5828	-1.2511
Mean	0.1691	0.0842	0.3392
Standard Deviations	0.9180	1.0769	0.8617

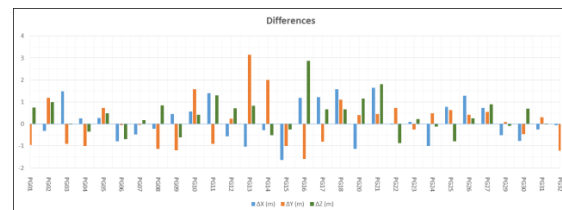


Figure 5 : Differences of ECEF satellite coordinates computed from broadcast ephemerides from IGS final ephemerides

When Table 8 is examined, it is seen that the

differences between the coordinate components of broadcast and final ephemerides vary between $-1,6321$ m and $+1,6391$ m on the X-axis, between $-1,5828$ m and $+3,1444$ m on the Y-axis and between $-1,2511$ m and $2,8692$ m on the Z-axis. When the means of these differences are taken into consideration, it appears that X coordinate component has an average difference of ~ 17 cm, Y coordinate component ~ 8 cm, and Z coordinate component ~ 34 cm. On the other hand, when the standard deviations of computations are taken into consideration it can be seen from Table 8 that the mean standard deviation values are $0,9180$ m, $1,0769$ m, $0,8617$ m for X, Y and Z components, respectively.

Numerous studies have been conducted from past to present with regard to orbital accuracy and its improvement. FGCC (Federal Geodetic Control Committee) stated in a guidebook entitled Geometric Geodetic Accuracy Standards and Specifications for Using GPS Relative Positioning Techniques published in 1989 that there were small differences between final ephemerides and broadcast ephemerides and that this accuracy was enough to meet the needs of most engineering projects. According to Rui-xi et al. (2014), accuracy of broadcast ephemerides was found to be around ± 1 m for each of the X, Y and Z coordinates. Likewise, it was stated in Grzegorz et al. (2015) and in IGS (2017) that satellite coordinates could be obtained with an accuracy of ± 1 m through broadcast ephemerides.

5. CONCLUSION

Reliable, consistent positioning accuracy has always driven new product development in the survey and mapping sector of the GNSS market (Cameron 2015). It should not be forgotten that accuracy of the coordinates calculated from broadcast and final ephemerides data is influenced by gravity field information and tropospheric and ionospheric factors. ITRF system, which uses GRS80 reference ellipsoid, is used in productions made from final ephemerides whereas WGS84 system, which again uses GRS80 reference ellipsoid in calculations made from broadcast ephemerides data, but it is pointed out that there is not much difference between WGS84 and ITRF systems in practical applications (Stanaway 2007).

When all the effects are taken into consideration, the desired precision (sensitivity) in the study to be conducted needs to be determined properly before deciding on the ephemerides information to be used. Use of IGS final ephemerides data in specific studies such as establishment of first degree Networks and deformation measurements which require extremely high precision may ensure that results have even higher levels of accuracy. For example, it would be appropriate to use IGS final ephemerides data to improve accuracies of ITRF coordinates of local/regional geodetic studies. On the other hand, release period of IGS products ranging from about 1 day to 2 weeks is a major disadvantage for high precision GNSS processing. Therefore, the fact that broadcast ephemerides data can be accessed at any time and that it yields results that are not much different from those obtained from final ephemerides data render

broadcast ephemerides a more easily applied alternative in many practical applications.

REFERENCES

- Bidikar, B., Rao, G.S., Ganesh, L., Santosh Kumar, MNVS., 2014. Satellite Clock Error and Orbital Solution Error Estimation for Precise Navigation Applications. Positioning, 2014, 5, 22-26
- Cameron, A., 2015. "More, More, More. Accuracy, Accuracy, Accuracy." GPS World, September 2, 2015, [Access Date; 14.08.2017]
- Federal Geodetic Control Committee (FGCC), 1989. Geometric Geodetic Accuracy Standards and Specifications For Using GPS Relative Positioning Techniques. Federal Geodetic Control Committee, Version 5.0, p.48.
- Grzegorz, N., Mariusz, F., Zofia, B., 2015. Comparison of GPS Precise Ephemerides Interpolation Methods. 15th International Multidisciplinary Scientific GeoConferences SGEM2015, Section Geodesy and Mine Surveying, pp 161-170, DOI: 10.5593/SGEM2015/B22/S9.020
- Hilla, S., 2010. The Extended Standard Product 3 Orbit Format (SP3-c). National Geodetic Survey National Ocean Service, NOAA, Silver Spring, MD 20910-6233, USA, <https://igsceb.jpl.nasa.gov/igsceb/data/format/sp3c.txt>, [Access Date; 24.07.2017].
- Hofmann-Wellenhof, B., Lichtenegger, H. and Collins, J., 1994. GPS – Theory and Practice. 3rd Edition, Springer-Verlag Wein New York.
- ICD, 1993. Interface Control Document – NAVSTAR GPS Space Segment/Navigation User Interfaces (ICD-GPS-200C). ARINC Research Corporation, Revision IRN-200C-004, 12 April 2000.
- IGS, 2017. International GNSS Service. <http://www.igs.org/>, [Access Date; 14.08.2017]
- Kahveci, M., Yildiz, F., 2001. Global Positioning System Theory-Applications. Nobel Publisher, p.184, Ankara, (in Turkish).
- Parkinson, B., Spilker, J. 1996. Global Positioning System: Theory and Applications. American Institute of Aeronautics and Astronautics, Volume U, p.643, Washington D.C.
- Remondi, BW. 1991. NGS Second Generation ASCII and Binary Orbit Formats and Associated Interpolated Studies. Proceedings of the Twentieth General Assembly, International Union of Geodesy and Geophysics, Vienna, Austria, August 11-24, 1991, 28 pp.
- Rui-xi, J., Xiao-yu, L., Chang-feng, X and Dong-yang, J., 2014. Broadcast Ephemerides Accuracy Analysis for GPS Based on Precise Ephemerides, Applied Mechanics and Materials Vols 602-605 (2014), pp 3667-3670.

Seeber, G., 1993. *Satellite Geodesy: Foundations, Methods, and Applications*. W. De Gruyter, p.531, Berlin, New York.

Stanaway, R., 2007, *GDA94, ITRF & WGS84 What's the difference? Working with Dynamic Datums, SSC 2007*, Hobart, Tasmania, Australia

Tusat, E., Turgut. B., 2003. *GPS Ephemerides Effects of Relative Positioning on the Coordinates and Baseline Components*. Selcuk University Journal of Engineering, Science and Technology, Vol.19, No.1, pp:65-72, Konya, (in Turkish).

Warren, DLM., 2002. *Broadcast vs Precise GPS Ephemerides: A Historical Perspective*. Master Thesis, Department Of The Air Force Air University Air Force Institute Of Technology, p.169, Ohio, USA.

Yoon, S., 2015. *Precise GPS Orbit Determination at National Geodetic Survey: How and Why*. 55th Civil GPS Service Interface Committee (CGSIC) Meeting, At the Institute of Navigation GNSS+ 2015 Conference Tampa Convention Center 14-15 September 2015, Tampa, Florida.

Copyright © International Journal of Engineering and Geosciences (IJEG). All rights reserved, including the making of copies unless permission is obtained from the copyright proprietors.



*International Journal of Engineering and Geosciences (IJEG),
Vol; 3; , Issue; 1, pp. 020-035, February, 2018, ISSN 2548-0960, Turkey,
DOI: 10.26833/ijeg.357161*

RADIOMETRIC IMPACT ASSESSMENT AROUND TWO QUARRY SITES, BENIN-OWO EXPRESS WAY, SOUTHWESTERN NIGERIA

Ademila, O.

Adekunle Ajasin University, Science Faculty, Department of Earth Sciences, Akungba Akoko, Nigeria
(omowumi.ademila@aau.edu.ng)

ORCID 0000 – 0001 – 5177 – 1110

*Corresponding Author, Received: 23/11/2017, Accepted: 30/12/2017

ABSTRACT: Total reliance on quarry products as construction materials has prompted commercial quarry activities globally. However, potential risks introduced by radiation exposure to quarries in two different locations in Ondo State, Nigeria were assessed to evaluate the background radiation and distribution of naturally occurring radionuclides associated with these areas. A ground radiometric mapping of eleven traverses across the two quarry sites was carried out using Gamma ray spectrometer. Naturally occurring radionuclides ^{238}U , ^{232}Th and ^{40}K in natural quarried materials of coarse rock aggregates and soil samples collected at a maximum depth of 2 m and up to 500 m away from the quarry sites were measured using gamma spectrometry method. Spectrometric data were processed and presented in form of radiometric maps showing the distribution of radiation level in each location. Results show that activity concentrations varied from one location to another. The radiation level in the recently quarried coarse rock aggregates (QF1 and QF2) (372 cps and 382 cps) are higher than the previously quarried coarse rock aggregates (QP1 and QP2) (365 cps and 377 cps) of the quarry sites. Activity concentrations in soils are in the order $^{232}\text{Th} < ^{238}\text{U} < ^{40}\text{K}$. The mean radioactivity concentration values of ^{232}Th , ^{238}U and ^{40}K are 0.0027 ± 0.0003 Bq/kg, 0.028 ± 0.0012 Bq/kg, 47.45 ± 0.0313 Bq/kg and 0.0036 ± 0.00036 Bq/kg, 0.026 ± 0.0012 Bq/kg and 69.42 ± 0.0313 Bq/kg respectively for soils within the quarries. At 500 m away from the quarry sites, mean values are 0.0008 ± 0.75 Bq/kg, 0.020 ± 0.0012 Bq/kg, 41.54 ± 0.0313 Bq/kg and 0.0049 ± 0.0004 Bq/kg, 0.052 ± 0.0012 Bq/kg and 200.32 ± 0.0313 Bq/kg respectively. The radiological hazard indices calculated were used to assess the health implication of exposure to rock aggregates and soil of the study areas. The values obtained when compared with their corresponding world permissible values were found to be below the internationally recommended values. Therefore, the level of radiation and interaction with the rock aggregates and soils do not expose the workers and people within and around the quarries to health problem. Hence, the quarry products can be used as building material for housing and road constructions.

Keywords: Quarries, Radiometric mapping, Radionuclides, Hazard indices, Rock aggregates

1. INTRODUCTION

Unwholesome activities of man have led to environmental degradation and health hazard of different kinds. Human exposure to background radiation originated from natural and man-made sources. Naturally occurring radionuclides contribute significantly to the exposure of human for radiation. The commonest of these radionuclides are the radioactive isotope of potassium ^{40}K and the radionuclides originated from the decay of ^{238}U and ^{232}Th series, both widely distributed in soil and rocks of the earth's crust. Natural environmental radioactivity concentrations and the associated external exposure due to gamma radiation depend mainly on geological and geographical conditions and appear at different levels in soils of each region in the world (UNSCEAR, 2000). Monitoring the terrestrial background radiation is very important due to the activity concentration of natural radionuclides in soil. When rocks are disintegrated through natural process, radionuclides are carried to soil by rain and flows (Taskin et al., 2009).

Quarrying operations have hazard effects on workers. Higher radiation levels are associated with igneous rocks, such as granite, and lower radiation levels with sedimentary rocks. Working activities carried out in quarries is a source of potential exposure because of natural radioactivity high levels arising from a large amount of primary radionuclides in the ^{238}U and ^{232}Th series and ^{40}K . A worksafe study has estimated that 2200 people die each year from various illnesses such as silicosis, pneumoconiosis and cancers caused by or associated with exposures to hazardous substances in the workplace. This is 4 to 5 times higher than the number of deaths from traumatic injury and so control of hazardous substances must be given highest priority (David, 1998). Quarrying activity involves mostly blasting and crushing of granite rocks and generates a lot of dust when processing. Dusts are one of, if not the major hazard to health from substances in quarries. Dust is generated at all stages of the production process and the smallest, indeed invisible particles are the most hazardous due to their ability to reach the lower part of the lung (the alveole). The most widely recognized hazardous component of the dust is crystalline silica which due to excessive exposure can cause severe respiratory problems or even silicosis and cancer. None of the commonly quarried rocks can be guaranteed silica free. Rocks classified as limestone have been shown to contain up to 40% crystalline silica and granite 55% crystalline silica. Quartzites and natural sands are normally in the range 80 – 100% crystalline silica. Exposure to silica dust during stone cutting in quarries carries the risk of development of silicosis, progressive massive fibrosis, asthma, chronic obstructive pulmonary disease, and airways obstruction in exposed workers (James, 2013). These airborne dusts (1 μm to 100 μm in diameter) are mainly in the form of particulates, which produced through the mechanical processes such as breaking, grinding and pulverizing, and the primary route of exposure is inhalation (Tim et al., 2004).

Studying the levels of radionuclide distribution in the environment provides essential radiological information.

Many sicknesses and diseases manifest after repeated and long exposure to radiation have been attributed to other sources and the nature and severity of the symptoms depend on the absorbed dose and the dose rate of radionuclides. Unfortunately, the sickness may take years to become evident, and indeed, when manifest it may already be too late. Hence, the knowledge of the natural radioactivity concentration of our environment is essential in the assessment of the degree and extent of radioactive contamination or pollution in the environment. In the quarrying industry, some of the most significant exposures to hazardous substances might be associated with the interaction of ionizing radiation with the human body, dust generated in the process or with fumes from vehicle exhausts and use of explosives. All these lead to various biological effects which may later show up as clinical symptoms. Data regarding levels of natural radioactivities in soils, rocks and the corresponding radiation doses to the people are lacking for most parts of Nigeria, as soil and rock radioactivity is also affected by man-made activities. The present study is necessitated on the need for protection from environmental pollution arising from environmental radioactivity, migration and evolution of radionuclides. So, this study was undertaken to evaluate the natural radionuclides activities of ^{238}U , ^{232}Th and ^{40}K in order to assess the background radiation and distribution of these radionuclides in the soils and rocks in the vicinity of two quarries in Ondo State and to determine the radiological impact of these nuclides on health of the workers and populace within and around these quarries with a view of appraising the environmental quality of the study areas. The radiological information would in-turn be used to determine whether a potential threat to human health in the environment exists that would warrant consideration of a remedial action.

2. LOCATION AND GEOLOGIC SETTING OF THE STUDY AREA

The study areas are Ebenezer Mining and Ceramics Company (Location 1) is situated in ancient city of Akure, Akure South local government area of Ondo State, Southwestern Nigeria. It lies within latitudes $7^{\circ} 10' \text{ N}$ and $7^{\circ} 19' \text{ N}$ and longitudes $5^{\circ} 07' \text{ E}$ and $5^{\circ} 14' \text{ E}$ (Fig. 1). It covers an area extent of about 1.5 km^2 and it's easily accessible to other major and urban centres in the state. It is bounded by Owo to the east, Ado –Ekiti to the north and Ondo to the south, all within 50 km radius. Within 100 km radius, it is bounded by Ikare, Ikole Ekiti, Ijere Ekiti to the north and Okitipupa to the south.

Ballister Mining Company (Location 2) is found on kilometer 20, Owo-Benin express way in Ose local government area of Ondo State, Nigeria. It is situated on latitudes $7^{\circ} 01' \text{ N}$ and $7^{\circ} 02' \text{ N}$ and longitudes $5^{\circ} 42' \text{ E}$ and $5^{\circ} 44' \text{ E}$ (Fig. 1). It's bounded by major cities and town like Kabba to north, to the east by Benin City, and to the west by Akure. It is accessible by network of tarred and untarred roads. The towns are situated in the humid tropical region of Nigeria, characterized by alternating wet and dry seasons with a mean annual rainfall of over 1500 mm. They are also characterized with a fairly uniform temperature and high relative humidity. The areas are drained by three major rivers Ala, Ogbese and Ose which are seasonal. The rivers dominate the drainage system of

the study area and it's mainly dendritic. It has an average elevation of about 378 m.

The study area falls within the Precambrian Basement Complex rocks of southwestern Nigeria (Rahaman, 1989). The geological history of the areas is similar to the structural evolutions that had affected the Basement Complex of Nigeria. The study areas are underlain by migmatite-gneiss-quartzite complex of the West African Basement rocks, which forms part of the Pan-African mobile belt. Charnockites, grey gneiss, granite gneiss, porphyritic granite and migmatitic rocks are the predominant rock types in the study area (Fig. 2). Granite gneiss is the metamorphosed granites, widely distributed in the study area and it is of two types; the biotite rich gneiss and the banded gneiss. The biotite rich gneiss is fine to medium grained and show strong foliation trending westwards and is usually dark in colour. The banded gneiss show parallel alignment and alteration. It occurs mostly as hills, boulders and flat lying exposures which are dark to light grey in colour and porphyroblastic in texture. There are several quartzite intrusions cutting across the granite and other felsic and basic rocks.

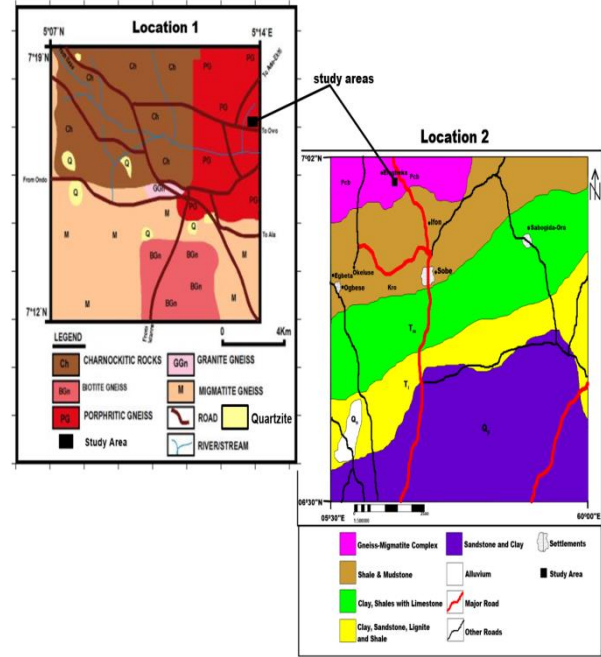


Figure 2: Geological map of the study areas.

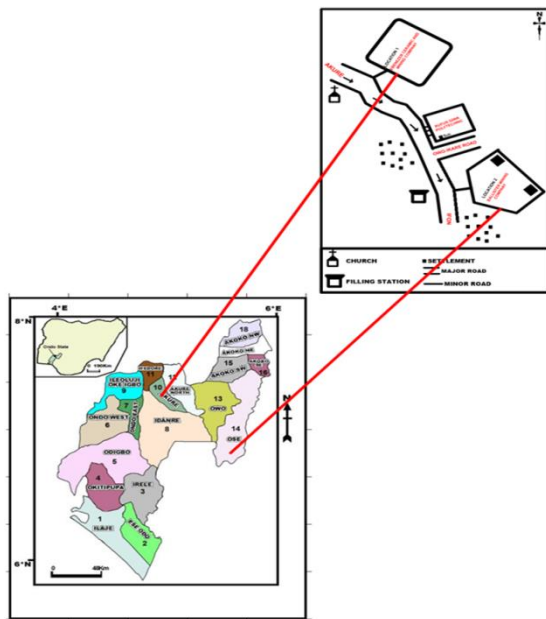


Figure 1: Map of Ondo State showing the location of the study areas.

3. MATERIALS AND METHODS

3.1 Gamma Survey

Measurements of radiations from rock aggregates were carried out at the quarries using one of the most cost effective and rapid techniques for geochemical mapping of radioactive elements. The rock aggregates are the coarse rock aggregates obtained from the freshly quarried rock boulders and coarse aggregates obtained from the previously quarried rock boulders. Measurements of the radioactive emission (gamma rays) emanating from the rocks are detected by a spectrometer, which counts the number of times each gamma ray of particular energy intersects it. The energy spectrum measured by the gamma ray spectrometer is in the range 0 – 3 MeV and energies of geological interest lie between 0.2 and 3 MeV. Peaks in the spectrum can be attributed to potassium, thorium and uranium, while the number of gamma ray counts across the whole spectrum is known as Total Count (TC) (Milsom, 2003). The gamma count is a function of the concentration of radioactive elements in rocks.

A highly portable hand held detector Gamma Ray Spectrometer was used for the measurements at 249 different points along eleven traverses (Fig. 3) around the two quarry sites with 5 m separation between points. The instrument always measures the complete spectrum, from which it evaluates the cps values and calculates the concentrations of elements K in (%), eU in (ppm) and eTh in (ppm). The measurements were carried out by positioning the spectrometer at the targeted sample located at varying distance from the quarry sites established by Global Positioning System (GPS). For each measurement, the background radiation level was recorded. Specific levels of activity concentration are related to the geological nature of rocks from which the soils originate. At each point, two readings were taken and the average

values calculated at each point is considered. The background reading was then subtracted from the mean value to obtain the actual mean radiation levels emitted by each sample. On the site measurements of radiations involve different coarse rock aggregates (coarse aggregates obtained from the freshly quarried rock boulders at the two quarry sites (QF1 and QF2) and coarse aggregates obtained from the previously quarried rock boulders at the two quarry sites (QP1 and QP2). The average values were used for the K (%), U (ppm), Th (ppm), Dose rate, Absorbed Dose rate, Effective Dose rate (outdoor and indoor), annual gonadal equivalent dose and Excess Lifetime Cancer Risk. The results are presented as means and standard deviations, plotted for pictorial view, representation and bar chart illustrations which determine the significant relationships between the radiations from the different types of sample. The results of the Total Count (TC) with their coordinates for all traverses in each locality were imported into Oasis Montaj™ (Grid and Image tool in Geosoft® software), the total count images were created after micro-levelling the entire data set to remove any apparent residual errors. These images were generated by employing mini-curvature gridding. A Ternary RGB colour models were produced from the software, from which potassium, thorium and uranium were assigned to the green, red and blue respectively because the blue tends to reduce the poorest signal-to-noise ratio of uranium channel.

3.2 Soil Sample Collection and Preparation

A total of 20 soil samples were collected from the study areas, 10 samples from each location (Fig. 3). Out of the 10 samples taken from each location, two samples each from four positions were taken at 500 m away from the quarry sites (Fig. 3). The measurement of radiation from subsurface soils was carried out directly inside the manually dug pits at a depth of 1 m to 2.0 m. That is, the gamma ray spectrometer was employed in recording in-situ the radioactivity measurement at the point of each sample collection to determine the exposure rate due to background radiation. The soils of the study areas are generally lateritic with some clay intercalation. About 2 kg soil samples were collected in polythene bags and labeled according to the quarry site and location and the GPS coordinates of the locations were recorded. The samples collected were then transported to the laboratory for further processing. The samples were processed following the standard procedures (EML, 1983). The samples were air-dried at room temperature for a week. Then milled and sieved through 2 mm sieve. They were weighed, sealed and stored in the laboratory for four weeks before being analyzed to ensure secular equilibrium between the various radioactive daughters involved. Proper sealing was ensured by providing double seal to the lid of the container.

3.3 Gamma Spectrometry and Determination of Activity Concentration

A gamma spectrometry system was employed in determining the activity concentrations of the radionuclides in the samples. All the samples were counted for 36,000 seconds (10 hours) and the peak areas corresponding to 1460 keV for ⁴⁰K, 352 keV (²¹⁴Pb) for ²³⁸U, and 583 keV (²⁰⁸Tl) for ²³²Th were considered for the

estimation of natural radionuclides in all the samples. The integrated counts recorded under the chosen energy peaks were noted for each spectrum. The specific activity concentration of each radionuclide in the samples was obtained using the comparative method of analysis. In this method, the activity concentration of the sample is determined by comparing the relevant peak area in the sample with area of similar photopeak in a reference standard with already known activity concentration. The activity concentration (C) in Bq/kg of the radionuclides in the samples was calculated after decay correction using the expression:

$$C_s \text{ (Bq/kg)} = C_a / \epsilon_\gamma \times M_s \times t_c \times P_\gamma$$

Where C_s = Sample concentration, C_a = net peak area of a peak at energy, ϵ_γ = Efficiency of the detector for a gamma energy of interest, M_s = Sample mass, t_c = total counting time, P_γ = the abundance of the gamma line in a radionuclide.

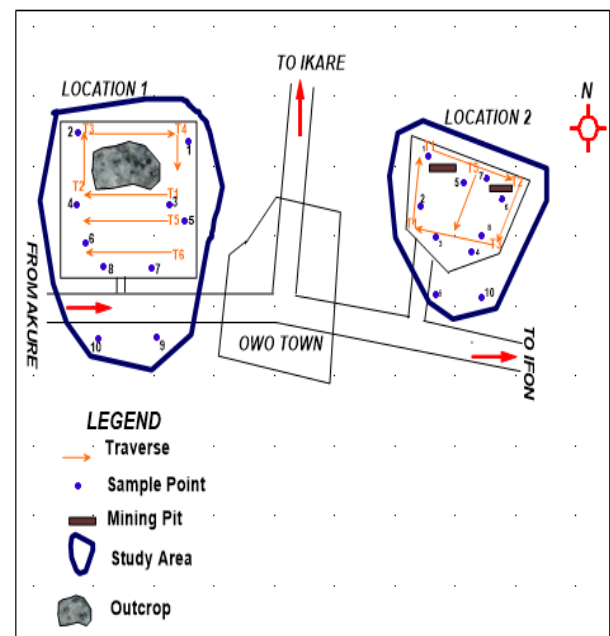


Figure 3: Data acquisition map of the study areas showing radiometric transverses and soil sample points

3.4 Assessment of Radiation Hazards

In order to assess the radiological impact of the investigated radionuclides in rock aggregates and the soil samples, the knowledge and estimation of the following radiation hazard parameters (indices) are important.

3.4.1 Radium equivalent activity (R_{eq})

The radium equivalent activity, R_{eq} is used to compare the specific activities of materials containing different quantities of ²³⁸U, ²³²Th and ⁴⁰K and the potential risk assessment associated with the radionuclides is estimated by calculating the radium equivalent activity (R_{eq}). It represents a weighted sum of activities of ²³⁸U, ²³²Th and ⁴⁰K. It is based on the assumption that 1 Bqkg⁻¹ of ²³⁸U, 0.7 Bqkg⁻¹ of ²³²Th and 13 Bqkg⁻¹ of ⁴⁰K produce the same

gamma radiation dose rates. The radium equivalent activity index was estimated using equation 1 (Avwiri et al., 2013) as shown in Tables 3 and 4.

$$R_{\text{aeq}}(\text{Bqkg}^{-1}) = C_U + 1.43C_{\text{Th}} + 0.077C_K \dots\dots\dots (1)$$

Where C_U , C_{Th} and C_K are the activity concentration in Bqkg^{-1} of ^{238}U , ^{232}Th and ^{40}K .

3.4.2 Air absorbed gamma radiation dose rate

Absorbed dose is a measure of the energy deposited in a medium by ionizing radiation per unit mass. It may be measured as joules per kilogram and represented by the equivalent S.I unit, gray (Gy) or rad. Effects of gamma radiation are normally expressed in terms of the absorbed dose rate in air, which originate from radioactive sources in the rock aggregates and the soil. The activity concentrations correspond to the total absorbed dose rate in air at 1 m above the ground level. The absorbed dose rate in air (D) for the workers in the quarry sites and the entire people living within and around the study areas is calculated using equation 2 and shown in Tables 2, 5 and 6. The gamma radiation doses can be estimated by employing the convenient formula (UNSCEAR, 2000).

$$D = (0.462 C_U + 0.621 C_{\text{Th}} + 0.0417 C_K) \text{ nGyh}^{-1} \dots\dots\dots (2)$$

Where: D is the absorbed gamma dose rates in air (nGyh^{-1}) at 1 m height above the ground level. C_U , C_{Th} and C_K represent the activity concentrations of ^{238}U , ^{232}Th and ^{40}K respectively. It is assumed that the contribution from other radionuclides, such as ^{137}Cs , ^{235}U , ^{87}Rb , ^{90}Sr , ^{138}La , ^{147}Sm and ^{176}Lu to the total dose rate are negligible. UNSCEAR reported that the world average absorbed gamma dose rate mean is 55 nGy/h.

3.4.3 Annual Gonadal Equivalent Dose (AGED)

The gonads, the bone marrow and the bone surface cells are considered as organs of interest by UNSCEAR (2000) because of their sensitivity to radiation. An increase in AGED has been known to affect the bone marrow, causing destruction of the red blood cells that are replaced by white blood cells. This situation results in a blood cancer called leukemia. The AGED received by the resident using such material for building can be evaluated by the following equation (Avwiri et al., 2012).

$$\text{AGED} (\mu\text{Sv/y}) = 3.09C_U + 4.18C_{\text{Th}} + 0.314C_K \dots\dots\dots (3)$$

Where C_U , C_{Th} and C_K are the radioactivity concentration of ^{238}U , ^{232}Th and ^{40}K in rock aggregates and soil samples.

3.4.4 Annual Effective Dose Equivalent (AEDE)

The annual effective dose equivalent (AEDE) received outdoor by a member of the public is calculated from the absorbed dose rate by applying dose conversion factor of 0.7 Sv/Gy and occupancy factor for outdoor and indoor was 0.2 and 0.8 respectively (Veiga et al., 2006).

$$\text{AEDE (Outdoor)} (\mu\text{Sv/y}) = D (\text{nGyh}^{-1}) \times T \times Q \times 0.2 \times 10^{-3} \dots\dots\dots (4)$$

Where D is the absorbed dose rate in air, Q is the conversion factor of 0.7 Sv/Gy, which converts the absorbed dose rate in air to human effective dose received and T is the time for one year, i.e. 8760 hrs.

$$\text{Thus, AEDE (Outdoor)} (\mu\text{Sv/y}) = D (\text{nGyh}^{-1}) \times 8760 (\text{hrs}) \times 0.7 (\text{Sv/Gy}) \times 0.2 \times 10^{-3} \dots\dots\dots (5)$$

$$\text{AEDE (Indoor)} (\mu\text{Sv/y}) = D (\text{nGyh}^{-1}) \times 8760 (\text{hrs}) \times 0.7 (\text{Sv/Gy}) \times 0.8 \times 10^{-3} \dots\dots\dots (6)$$

The AEDE indoor occurs within a house whereby the radiation risks due to use of the soil and rock as building materials are taken into consideration. AEDE outdoor involves a consideration of the absorbed dose emitted from radionuclide in the environment such as ^{238}U , ^{232}Th , ^{226}Ra and ^{40}K .

3.4.5 Representative Gamma Index (I_γ)

This is used to estimate the gamma radiation hazard associated with the natural radionuclide in specific investigated samples. The representative gamma index was estimated as follow (Avwiri et al., 2013).

$$I_\gamma = C_U / 150 + C_{\text{Th}} / 100 + C_K / 1500 \leq 1 \dots\dots\dots (7)$$

Where C_U , C_{Th} and C_K are the activity concentrations of ^{238}U , ^{232}Th and ^{40}K .

The representative gamma index must be lower than unity in order to keep the radiation hazard insignificant.

3.4.6 Hazard Indices (H_{ex} and H_{in})

External radiation hazard index (H_{ex})

External radiation hazards due to natural radionuclides of ^{238}U , ^{232}Th and ^{40}K are defined in terms of external or outdoor radiation hazard index, denoted by H_{ex} . The external hazard (H_{ex}) and internal hazard (H_{in}) indices were evaluated by the following relations (Ramamamy et al., 2009):

$$H_{\text{ex}} = C_U/370 + C_{\text{Th}}/259 + C_K/4810 \leq 1 \dots\dots\dots (8)$$

$$H_{\text{in}} = C_U/185 + C_{\text{Th}}/259 + C_K/4810 < 1 \dots\dots\dots (9)$$

Where C_U , C_{Th} and C_K are the radioactivity concentrations of ^{238}U , ^{232}Th and ^{40}K in BqKg^{-1} respectively.

H_{in} should be less than unity for the radiation hazard to be negligible. Internal exposure to radon is very hazardous which can lead to respiratory diseases like asthma (Tufail et al., 2007). Natural radionuclide in soil, rocks and sediment produce an external radiation field to which all humans are exposed. H_{ex} must be less than unity for this external radiation hazard to be negligible (Beretka and Mathew, 1985). H_{ex} equal to unity corresponds to the upper limit of radium equivalent dose (370 Bqkg^{-1}) (Beretka and Mathew, 1985).

3.4.7 Excess Lifetime Cancer Risk (ELCR)

This is the probability of developing cancer over a lifetime at a given exposure level, considering 70 years as the average duration of life for human being. The Excess

Lifetime Cancer Risk (ELCR) was calculated using the following equation (Taskin et al., 2009).

$$ELCR = AEDE \times DL \times RF \dots\dots\dots (10)$$

Where AEDE is the Annual Equivalent Dose Equivalent, DL is the average duration of life (estimated to 70 years) and RF is the Risk Factor (Sv^{-1}), i.e. fatal cancer risk per Sievert. For stochastic effects, ICRD uses RF as 0.05 for public (Taskin et al., 2009).

3.5 Conversions

The elemental concentrations of uranium-238 (ppm), Thorium-232 (ppm) and potassium-40 (%) can be calculated from measured activity concentrations of ^{238}U , ^{232}Th and ^{40}K in $Bqkg^{-1}$ using conversion factors recommended by the IAEA, 2003 as follows:

$$1 \text{ ppm} = 10^{-4}\% \dots\dots\dots (11)$$

$$1\% \text{ K} = 313 \text{ Bqkg}^{-1} \text{ of } ^{40}K \dots\dots\dots (12)$$

$$1 \text{ ppm U} = 12.35 \text{ Bqkg}^{-1} \text{ of } ^{238}U \dots\dots\dots (13)$$

$$1 \text{ ppm Th} = 4.06 \text{ Bqkg}^{-1} \text{ of } ^{232}Th \dots\dots\dots (14)$$

In recent years, the SI (System International) units used in radiation protection are the Gray (Gy) and the Sievert (Sv). The Gray is the unit of absorbed dose corresponding to the rad and is the energy imparted by ionizing radiation to material corresponding to one joule/kg, while the Sievert is the unit of dose equivalent corresponding to the rem.

4. RESULTS AND DISCUSSION

Granite rocks are older granite suite of the Basement Complex rocks known to be associated with elevated levels of naturally occurring radionuclides and emit ionizing radiation to the environment of the quarry. Thus, workers and residents around such site are liable to radiation exposure. Due to this, it is important to measure the rates of radiation exposure around quarry sites to safe lives of this category of people.

The radiometric data around the quarry sites are summarized in terms of colour images (radiometric images) obtained from minimum curvature grids. Figures 4 and 5 show the radiometric data in terms of Total Count (TC) which is a measure of total radioactivity over the spectrum. The images shown use an equal-area normalization of the colour scale. The data indicate the composite radiogenic activity of the formations around the quarry sites. It is evident that there is a significant geological control of the radiometric responses observed. The contributions from the three radioelements; potassium, uranium and thorium are summarized in the ternary image (Figs. 4d and 5d). The ternary image is a normalized (to an equal-area histogram) 3-way colour stretching of the contributions from the individual radioelements. The presentation is a standard method in radiometric processing and interpretation (IAEA, 1991). In areas where all three radioelements concentrations are low, the ternary image shows black, when all the three concentrations are high, the ternary response tends to white. The three radiogenic elements highs and lows in the ternary image are also reflected in the high and low zones

within the Total Count (TC) images. From the ternary map, the weathered rock can easily be delineated as having low concentration of the three radiogenic elements (depicted by a black colour in Figs. 4d and 5d).

4.1 Radiometric Maps (Location One)

In order to have better understanding of the distribution and distinctness of the different level of radiations emitted from the rock types in the study areas, image maps and ternary characters of the radioelements (K, U and Th) are shown in Figs. 4 and 5.

4.1.1 Potassium map

The potassium, K map (Figure 4a) shows different degrees of potassium concentrations that reflect different lithological units and alterations in the area. Potassium radiation fundamentally comes from potash feldspars, which are mainly common in felsic igneous rocks (e.g. granite) and are low in mafic rocks (e.g. basalts and andesite) (Gunn et al., 1997b). Rock alterations can also result in high K concentrations (Wilford et al., 1997). A number of potassium anomalies are evident in the radiometric image Fig. 4a. The blue colour corresponds with low K values while the pink corresponds with very high K values. The colour red represents moderately high to high K values and the shades of orange to yellow colour are associated with moderately low K values. Low potassium concentration is observed at the southeastern (E) part of the image, similar observation is seen around the central part of the image (G, H, D) and a fairly low concentration is also observed in the southwestern part (G) of the map. This Low concentration might be as a result of the type of soil within this region which is lateritic soil with clay intercalations with high water retaining capacity. This tends to shield the potassium radiation from the underlying rocks hence, reducing the intensity of the signal at that point. Since radiometric survey uses the assumption that residual soil of top 30 cm is able to absorb most of the radiated radioactive element from the underlying rocks or the lithology. To justify this, the fairly low concentration observed on the southwestern part of the image corresponds to the mining phase, hence does not contain much water to release to the surrounding. The low K in location 1 could be attributed to the geologic materials in the lineaments and also as a result of the ore body present in the environment. High concentration of potassium is also observed at the northwestern and southwestern parts of the Location (Fig. 4a).

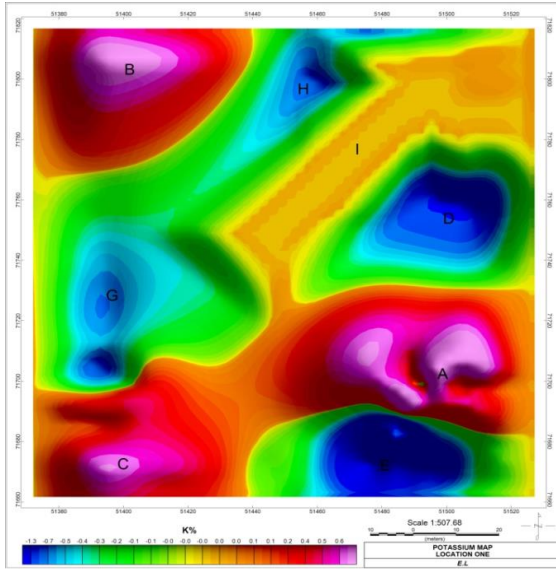


Figure 4a: Map showing the concentration of potassium in entire area of Location 1

4.1.2 Thorium map

The thorium map shows three distinct regions of thorium concentration in the area. The pink colour represents high concentration of the thorium and low thorium concentration represented by blue colour (Figure 4b). The high concentration in thorium depicted A (Figure 4b) corresponds to acid intrusive rock in the area. An enrichment of thorium may be indicative of alteration of natural processes in the areas. In addition, the low concentration of Th (E, H, I, J, K) observed towards the northern and southern parts on the Th map of the area coincides with the weathered rocks in the area. This indicates the fact that the water body shields the emission of radiation from radiogenic element (thorium) of the underlying lithology.

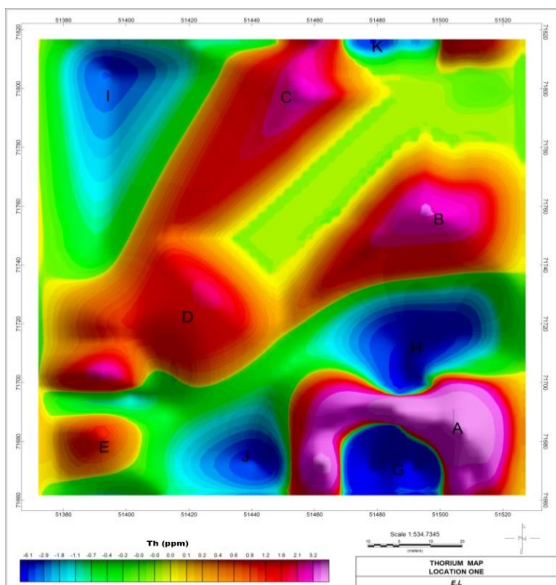


Figure 4b: Thorium concentration map of Location 1

4.1.3 Uranium map

The uranium image shows good definition in mapping felsic rock, highest content of silicon with predominance of quartz, alkaline feldspar e.g granite, rhyolite and weathered sediments (radiogenic pattern D and H in Fig. 4c) and certain radiogenic rock pattern A, B and G. The feature marked A, registered high uranium concentration. High concentration of uranium is also observed at the northeastern and southeastern parts of the area, and fairly low concentration of uranium at the northwestern part of the map. This feature coincides with granite in the area. Thus the granite is broadly represented by high U concentration. Unlike the K and Th maps, the uranium map could not clearly delineate the distinct boundary between most of the lithology of the area. At the eastern part of the map in (Figure 4c), there exists noticeable halos. This halo is attributed to rock alteration like weathering in that region. The low U in the study area is also as a result of the underlying geology attributed to the area.

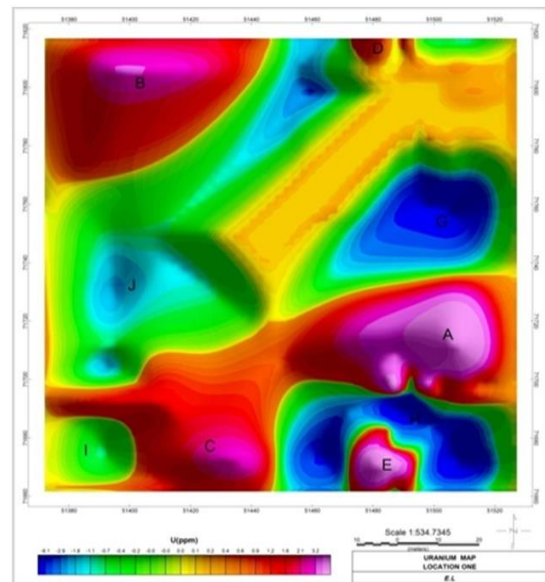


Figure 4c: Uranium concentration map of Location 1

4.1.4 Ternary Map

The ternary map of K- eTh- eU parameters (Fig. 4d) shows interaction of three radionuclides in the definition of the contacts of the map and the borders of the nucleus. Green indicates predominance of Thorium over the other two radioelements. Low concentrations of U, Th, and K radioactive elements are displayed by black colours, with the magenta colour (A and G) corresponding to high potassium with low uranium and thorium concentrations, this is observed at the central part of the image. Those with the low content of K but high contents of U and Th are represented by green colour (B, H and I) and the yellow colour (D) are characterized by high potassium and thorium with low uranium. Additionally, the blue colour (C) corresponds to regions of high uranium with low potassium and thorium and white colour corresponds to high potassium, uranium and thorium. From the ternary map, the weathered rock was delineated as having

low concentration of the three radiogenic elements (depicted by a black colour in Fig. 4d). The high concentration of K, Th and U (A) of western part of the image coincides with granite unaltered in the area. The high K with low U and Th concentration which is depicted by a magenta colour coincides with granitic rock. Blue colour corresponds to regions of high uranium with low potassium and thorium which may be attributed to unearthed intrusive igneous rock in the area.

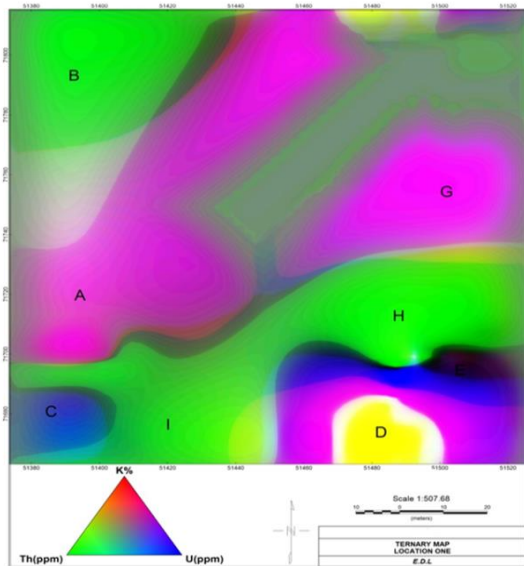


Figure 4d: Ternary map of Location 1

4.2 Radiometric Maps (Location Two)

4.2.1 Potassium map

Areas of high values of potassium are due to mineralogical compositions of the rocks as observed in the northeastern part of the map (A) (Fig. 5a), where a homogeneous gamma spectrometric pattern is noticed. The low concentration of potassium in the rocks of the study area is due to their basic composition. The low values of potassium are interpreted as been related to altered rock, which is an indication of loss of potassium due to weathering. High potassium values in the northeastern region of the map are observed along an alignment AA probably related to a fault.

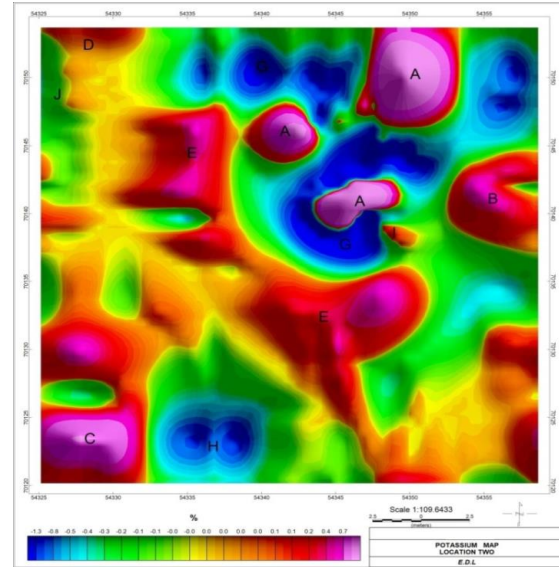


Figure 5a: Map showing the concentration of potassium in Location 2

4.2.2 Thorium map

Thorium tends to be restricted to clays colloids and iron oxides forming anomalous concentration without any geological correlation. Anomalies in the thorium, maps the lithology and lithological boundaries of the area. The thorium (Th) map shows three distinct regions of thorium concentration in the area. Relatively high concentrations of Th are represented by pink colour and low Th concentrations are represented by blue colour (Fig. 5b). The high concentration in Th depicted (A) in southwestern, (B) in northeastern region of the map (Fig. 5b) is attributed to the absence of undeformed potassic feldspar minerals in the area. This could also have resulted from the terrestrial gamma radiation or due to incorporated minerals from the surrounding rocks. Moreover, the low concentration of Th (G, M) observed at the northern region of the map and (K, I) southwestern part of the area coincides with the biotite and weathered rocks in the area. This indicates that the water-body shields the emission of radiation from radiogenic element (thorium) of the underlying lithology. This also indicates that the rock/residual soil has low terrestrial gamma radiation or emission due to geologic processes.

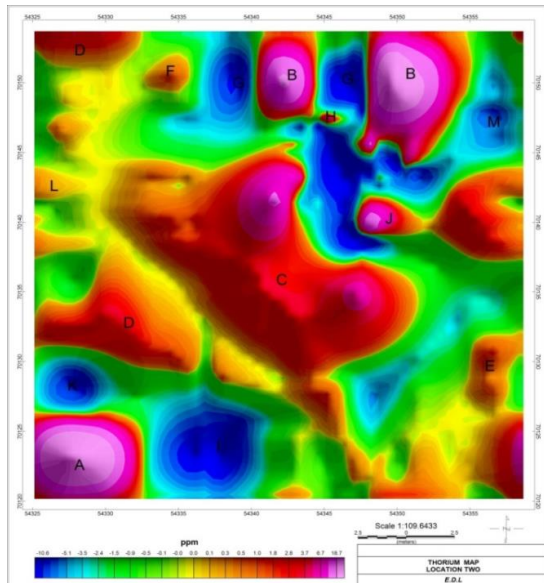


Figure 5b: Map showing the concentration of thorium in Location 2

4.2.3 Uranium map

High concentration of uranium towards the northern part (Fig. 5c) is interpreted as an indication of areas sufficiently concentrated in clays and iron oxides. Areas of intermediate uranium value can be observed in southern part of the area of Location 2. Enriched zones can be related to deformation processes in which uranium-rich fluid are mobilized. Figure 5c shows great variability of uranium grades, probably because of pedogenetic phenomena.

4.2.4 The Ternary Image

The ternary map of K- eTh- eU parameters (Fig. 5d) shows interaction of three radionuclides in the definition of the map. The ternary radiometric map (Fig. 5d) shows different colour combinations which indicate the K, Th and U concentrations. Low concentrations of U, Th, and K radioactive elements are displayed by black colours with the magenta colour (C) corresponding to high potassium with low uranium and thorium concentrations. Those with the low content of K but high contents of U and Th are represented by green colour (H) and the yellow colours (C) are characterized by high potassium and thorium with low uranium. Additionally, the blue colour (E) corresponds to regions of high uranium with low potassium and thorium and white (D) colour corresponds to high potassium, uranium and thorium. From the ternary map, the areas with low concentration of the three radiogenic elements depict altered rocks due to the fact that radiogenic elements lose their concentration due to alteration (Fig. 5d). The high concentration of K, Th and U (portions marked by A) in the northeastern part of the ternary image coincides with unweathered granitic rock in the area. The high K with low U and Th concentration which is depicted by a magenta colour can be attributed to the fact that some areas around the quarry site have not been exploited, that is, quarry activities which involve bringing the naturally occurring radioactive materials to the surface have not taken place. This can be corroborated

with the presence of some local indigenous tress found within the areas. Blue colour corresponds to regions of high uranium with low potassium and thorium which may be attributed to felsic schist- highly sheared granite in the area. Generally, the variation in the radioactivity of the study areas could be attributed to the rock types, especially low concentration is due to weathered nature/mineralogical compositions of the rocks. Also, the variations are always associated to acidic intrusive and metamorphosed rocks.

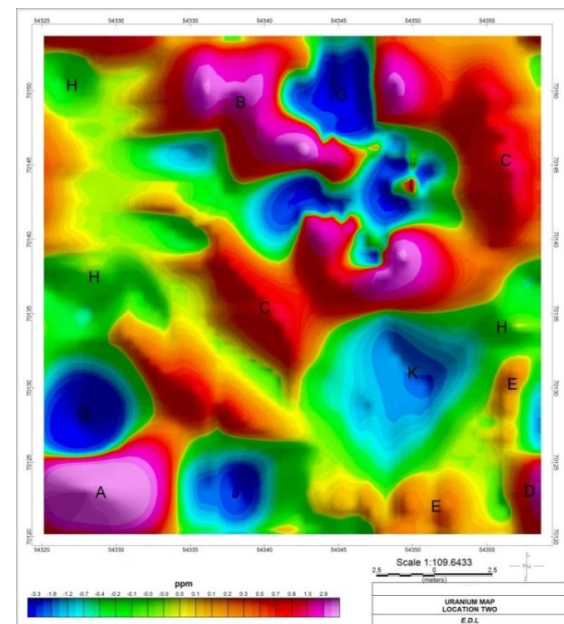


Figure 5c: Uranium concentration map of Location 2

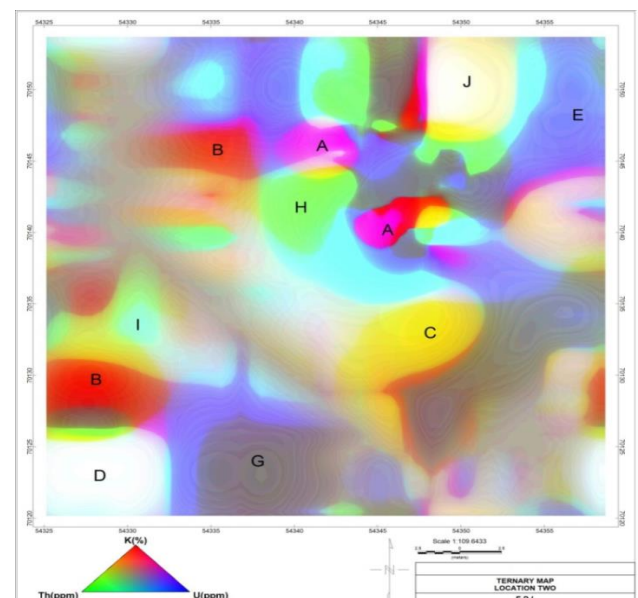


Figure 5d: Ternary map of Location 2

Investigations have shown that levels of radiations vary considerably based on soils, rock types and also in the types of radioisotopes. High radiation levels from natural radionuclide have been associated with granitic and silicic igneous rocks like those in the study area (Brimhal and

Adams, 1982). It is therefore possible that the measured radiation from the study areas are from the natural radionuclides like ^{238}U , ^{232}Th and ^{40}K which are the radioisotopes associated with igneous rocks. These rocks have been observed to be more radioactive than the metamorphic rocks (Brimhal and Adams, 1982). The radiation levels in the recently quarried coarse aggregate rocks at the quarry sites of Locations 1 and 2 (QF1 and QF2) are 372 cps and 382 cps (Table 1) with absorbed dose rates of 9.14 nGy/hr and 7.31 nGy/hr (Fig. 6) and annual effective dose rate of 11.21 $\mu\text{Sv/yr}$ and 8.97 $\mu\text{Sv/yr}$ (Table 2). Similarly, the radiation levels in the previously quarried coarse aggregate at the quarry sites of Locations 1 and 2 (QP1 and QP2) with absorbed dose rates and their annual effective dose rates are 365 cps and 377 cps (Table 1), 6.08 nGy/hr and 3.16 nGy/hr and 7.45 $\mu\text{Sv/yr}$ and 3.87 $\mu\text{Sv/yr}$ respectively (Table 2). The values of radiation of coarse aggregates obtained from the freshly quarried rock boulders (QF1 and QF2) and the previously quarried rock boulders (QP1 and QP2) at the two quarry sites were compared. It was observed that the values of radiations in the recently quarried coarse aggregate rocks are higher than the previously quarried coarse aggregate (Table 1). The higher values of radiation in the recently quarried coarse aggregate rocks at the quarry sites compared with the previously quarried coarse aggregate rocks are indicative of the fact that the radionuclides are resident in the parent rock materials. The mean absorbed dose measured ranged from 3.16 nGy/hr to 9.14 nGy/hr. The highest absorbed dose rate was recorded in recently quarried coarse aggregate rocks at the quarry site of Location 1, while, the least dose rate was obtained in previously quarried coarse aggregate rocks at the quarry site of Location 2 (Fig. 6). The mean values are lower than the world average value of 55 nGy/hr (Fig. 6). The corresponding outdoor and indoor mean annual effective doses ranged from 3.87 $\mu\text{Sv/yr}$ to 11.21 $\mu\text{Sv/yr}$ and 15.50 $\mu\text{Sv/yr}$ to 44.84 $\mu\text{Sv/yr}$ (Table 2, Figs. 7 and 8). The values of outdoor and indoor annual effective dose equivalent in

this study is far below the worldwide average annual effective dose equivalent values of 70 $\mu\text{Sv/yr}$ for outdoor and 450 $\mu\text{Sv/yr}$ for indoor annual effective dose equivalent (Figs 7 and 8). The results obtained for the annual gonad equivalent dose (AGED) (21.75 mSv/yr to 63.02 mSv/yr) and the excess lifetime cancer risk (ELCR) (0.014 to 0.039) (Table 2 and Fig. 9) are below the permissible values of 300 mSv/yr and 0.29×10^{-3} respectively (UNSCEAR, 2000). This implies that the gonadal values may pose no threat to the bone marrow and the bone surface cells of the workers and the general populace around the study areas.

The excess lifetime cancer risk estimated from the annual effective dose (Table 2) in the quarry sites fall below the world weighted average (Fig. 9) indicates that the probability of the workers and the people living around the vicinity to develop extra cancer due to exposure to natural radioactivity is insignificant right now, however, continuous accumulation may pose radiological health risks to the people living in the areas in future. Also, the calculated values of the external hazard index, internal hazard index and representative gamma index for rock aggregates studied are less than the world permissible value of unity (Fig. 9). This is an indication that the rock aggregates produced from these quarries will not introduce any respiratory tract disease such as asthma and other external diseases such as skin cancer, erythema and cataracts to the workers involved in quarry activities and users of such rock aggregates. Relatively higher value of radiations in coarse aggregates of porphyritic granite gneiss compared with the coarse aggregates of fine to medium grained banded gneiss in this study implies that fine to medium grained rocks absorb and reflect radiation easily than rocks of predominantly coarse grains. This shows that radionuclide distribution in rocks is influenced by grain size distribution. The study also shows that thorium has the highest contribution to the total absorbed dose in rock aggregates of the study areas.

Table 1: Total Mean Values of Radionuclides from Rock Aggregates from the Quarry Sites Environment

Location Code	Sample	Mean K (%)	Mean U (ppm)	Mean Th (ppm)	Mean Total Count (cps)	Dose Rate
QF1		1.03	2.3	13.3	371.7	59.8
QP1		0.40	2.4	8.2	364.7	39.6
QF2		3.85	1.1	11.0	382.2	84.4
QP2		4.66	2.1	3.3	376.7	81.6

Table 2: Radiation Hazard parameters for rock aggregates

Sample Code	Mean Absorbed Dose Rate (D) (nGy/hr)	AEDE (outdoor) ($\mu\text{Sv/yr}$)	AEDE (indoor) ($\mu\text{Sv/yr}$)	AGED (mSv/yr)	ELCR ($\times 10^{-3}$)	H_{ex}	H_{in}	I_{γ}
QF1	9.14	11.21	44.84	63.02	0.039	0.058	0.064	0.149
QP1	6.08	7.45	29.83	41.82	0.026	0.038	0.045	0.098
QF2	7.31	8.97	35.86	50.59	0.031	0.046	0.049	0.120
QP2	3.16	3.87	15.50	21.75	0.014	0.019	0.025	0.050

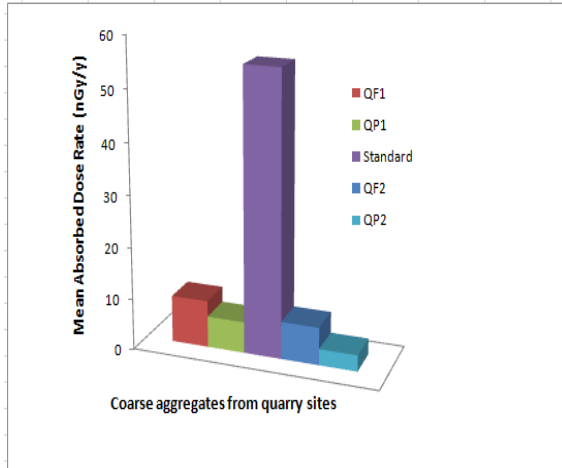


Figure 6: A comparison of the absorbed dose rate (nGy/h) in the study area. S is the standard threshold limit by UNSCEAR (2000)

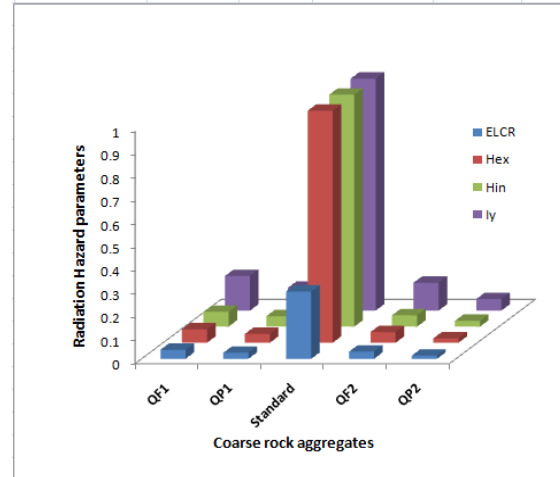


Figure 9: Excess Lifetime Cancer Risk, External hazard index, Internal hazard index and Gamma Representative Index in coarse rock aggregates of the study area as compared with the UNSCEAR, 2000.

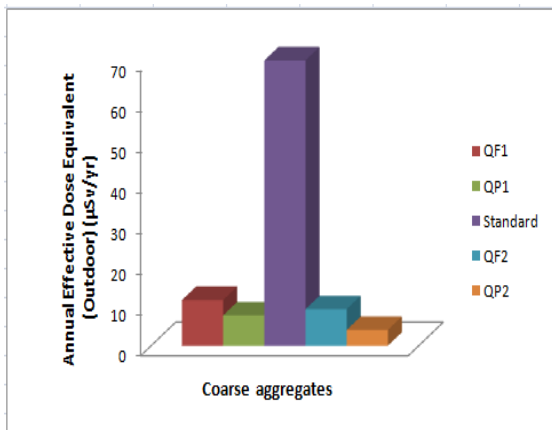


Figure 7: A comparison of the Annual Effective Dose Equivalent (outdoor) (AEDE) in coarse aggregates with the UNSCEAR, 2000

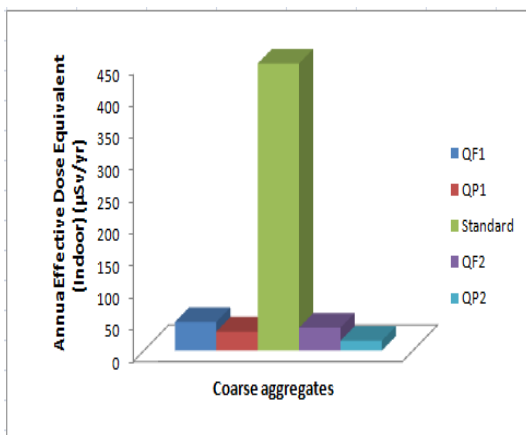


Figure 8: A comparison of the Annual Effective Dose Equivalent (indoor) (AEDE) in coarse aggregates with the UNSCEAR, 2000

The results of gamma-ray measurements of ^{238}U , ^{232}Th and ^{40}K activity concentrations of the quarries soil samples with their radium equivalent activity are given in Tables 3a and 4a, while that at 500 m away from the quarries are given in Tables 3b and 4b (Fig. 10). The activity concentrations vary from site to site, which indicates a large variation in chemical and mineralogical properties of soil samples. Activity concentrations are in the order $^{232}\text{Th} < ^{238}\text{U} < ^{40}\text{K}$. The mean radioactivity concentration values of ^{232}Th , ^{238}U and ^{40}K are 0.0027 ± 0.0003 Bq/kg and 0.0036 ± 0.00036 Bq/kg, 0.028 ± 0.0012 Bq/kg and 0.026 ± 0.0012 Bq/kg and 47.45 ± 0.0313 Bq/kg and 69.42 ± 0.0313 Bq/kg respectively for soils within the quarries of Locations 1 and 2 (Tables 3a and 4a). At 500 m away from the quarry sites, the mean values are 0.0008 ± 0.75 Bq/kg and 0.0049 ± 0.0004 Bq/kg, 0.020 ± 0.0012 Bq/kg and 0.052 ± 0.0012 Bq/kg and 41.54 ± 0.0313 Bq/kg and 200.32 ± 0.0313 Bq/kg respectively for the quarries (Tables 3b and 4b). The result shows that the activity concentration within the quarry site of Location 1 is higher than that at 500 m away from the quarry. This could be as a result of temperature, elevation difference and radioactive half-lives, while, the result of Location 2 shows that the activity concentration at 500 m away is higher than the activity concentration within the quarry site as shown in Fig. 10. Although, these activity concentration values obtained in these locations and their environs are below the world permissible value of 30.0 Bq/kg for ^{232}Th , 35.0 Bq/kg for ^{238}U and 400.0 Bq/kg for ^{40}K (UNSCEAR, 2000) (Fig. 10). Change in the soil activity with location depends on the soil physical and chemical properties which are common phenomenon in any appraisal of radiation in the environment. The spatial distribution of the radionuclides across the two locations revealed that the concentration of ^{40}K was highest even at the neighbouring settlement, making ^{40}K the dominant radionuclide in the areas (Fig. 10). The relatively high values of ^{40}K could be as a result of feldspathic characterization of rock formation of the study areas. ^{238}U and ^{232}Th has the lowest concentration. The low concentrations especially in some places of the study areas can be attributed to the presence of some local indigenous

trees around the sites, which shows that those areas have not been exploited. This corroborated with the result of the radiometric maps generated from the measurements of different points along eleven traverses around the study areas. Radium equivalent activity (Ra_{eq}) owing to activity concentration of the three natural radionuclides from the two sites varies from 0.70 to 28.94 Bq/kg. These values are below the world standard of 370 Bq/kg (Fig. 10).

The estimated absorbed dose rates in all the soils investigated ranged from 0.38 nGy/hr to 15.67 nGy/hr (Tables 5a, 6a and Fig. 11). The total absorbed dose delivered by these radionuclides for the soils within Location 1 ranged from 0.38 nGy/hr to 3.68 nGy/hr and 1.10 nGy/hr to 3.43 nGy/hr within Location 2, having average values of 1.99 nGy/hr and 2.91 nGy/hr respectively (Tables 5a and 6a). The estimated absorbed dose values for 500 m away from the quarry sites are shown in Tables 5b and 6b. The mean total absorbed doses obtained at 500 m away are 1.74 nGy/hr and 8.38 nGy/hr respectively for the two locations. All these values are less than the recommended world average value of 55 nGy/hr (Fig. 11). The differences arising from these values may be due to the geological settings of the area due to variation from one place to another and from one locality to another even within the same geographical area. The calculated values of annual effective dose ranged between 0.47 to 4.51 μ Sv/yr with mean value of 2.44 μ Sv/yr within Location 1 and 1.35 to 4.21 μ Sv/yr with mean 3.57 μ Sv/yr within Location 2 (Tables 5a and 6a). The mean values of effective doses obtained for 500 m away from the sites are presented in Tables 5b and 6b. It was found that the effective doses obtained at 500 m away (10.28 μ Sv/yr) from Location 2 is higher than that obtained at Location 1 (2.13 μ Sv/yr). The mean effective doses are far below the worldwide recommended limit for normal background

effective dose of 70 μ Sv/yr (Fig. 12). The mean values of annual gonadal equivalent dose (AGED) obtained within the sites are 15.00 mSv/yr and 21.89 mSv/yr, while, AGED calculated for 500 m away from each site are 13.11 mSv/yr and 63.08 mSv/yr respectively as shown in Fig. 13. These values are far below the safe limit of 300 mSv/yr (Fig. 13). This implies that interaction with the soils in the study areas poses no threat to the bone marrow and the bone surface cells of the workers and the populace around the study areas.

The range mean excess lifetime cancer risk (ELCR) calculated for the study areas is 0.009 to 0.067 (Fig. 14). These values are below the world standard of 0.29×10^{-3} (Taskin et al., 2009) meaning that the probability of the workers and the people living around the quarry sites developing extra cancer due to exposure to natural radioactivity is insignificant right now, however, continuous accumulation may pose radiological health risks to the people living in the areas in future. Also, the calculated values of the external hazard index, internal hazard index and representative gamma index for soils of the areas are less than the world permissible value of unity (Fig. 14). This indicates that interaction with the soils in the study areas will not result to any respiratory tract disease such as asthma and other external diseases like skin cancer, erythema and cataracts (Avwiri et al., 2013) to the workers involving in quarry activities and users of such soils. Generally, the relatively low gamma dose rates measured from the coarse aggregate rocks and subsurface soils of the two quarry sites show that quarry activities in the areas have not enhanced the background radiation level of the areas. This suggests that the rock aggregates and soils from these quarry sites can be used as building materials for housing construction without posing a health threat to the general public.

Table 3a: Specific activity of ^{40}K , ^{238}U and ^{232}Th and their radium equivalent in soil samples within quarry 1

Sample Code	K (Bq/kg)	U (Bq/kg)	Th (Bq/kg)	Raeq (Bq/kg)
EMC 1	43.75±0.0313	0.022±0.0012	0.0106±0.0004	3.4057
EMC 2	8.88±0.0313	0.011±0.0012	0.0011±0.0002	0.6961
EMC 3	22.37±0.0313	0.020±0.0012	0.0015±0.0003	1.7441
EMC 4	48.02±0.0313	0.044±0.0012	0.0004±0.0002	3.7418
EMC 5	33.84±0.0313	0.018±0.0012	0.0009±0.0002	2.6244
EMC 6	69.47±0.0313	0.051±0.0012	0.0011±0.0003	5.4015
EMC 7	65.59±0.0313	0.022±0.0012	0.0018±0.0003	5.0750
EMC 8	87.67±0.0313	0.040±0.0012	0.0039±0.0004	6.7965
Mean	47.45±0.0313	0.028±0.0012	0.0027±0.0003	3.6856

Table 3b: Specific activity of ^{40}K , ^{238}U and ^{232}Th and their radium equivalent in soil samples 500 m away from the quarry 1 locality

Distance (m)	Sample Code	K (Bq/kg)	U (Bq/kg)	Th (Bq/kg)	Raeq (Bq/kg)
500 m away (East)	EMC 9	45.43±0.0313	0.019±0.0012	0±0	3.5175
500 m away (West)	EMC 10	37.65±0.0313	0.022±0.0012	0.0015±1.4941	2.9231
	Mean	41.54±0.0313	0.020±0.0012	0.0008±0.7470	3.2203

Table 4a: Specific activity of ^{40}K , ^{238}U and ^{232}Th and their radium equivalent in soil samples within quarry of Location 2

Sample Code	K (Bq/kg)	U (Bq/kg)	Th (Bq/kg)	Raeq (Bq/kg)
BMC 1	77.39±0.0313	0.002±0.0012	0.002±0.0003	5.9639
BMC 2	25.70±0.0313	0.039±0.0012	0.009±0.0004	2.0304
BMC 3	81.92±0.0313	0.036±0.0012	0.003±0.0004	6.3485
BMC 4	71.45±0.0313	0.040±0.0012	0.002±0.0004	5.5447
BMC 5	78.54±0.0313	0.018±0.0012	0.001±0.0003	6.0676
BMC 6	70.02±0.0313	0.024±0.0012	0.001±0.0003	5.4170
BMC 7	80.68±0.0313	0.033±0.0012	0.003±0.0004	6.2491
BMC 8	69.68±0.0313	0.018±0.0012	0.008±0.0004	5.3954
Mean	69.42±0.0313	0.026±0.0012	0.004±0.0004	5.3771

Table 4b: Specific activity of ^{40}K , ^{238}U and ^{232}Th and their radium equivalent in soil samples 500 m away from the quarry 2 locality

Distance (m)	Sample Code	K (Bq/kg)	U (Bq/kg)	Th (Bq/kg)	Raeq (Bq/kg)
500 m away (East)	BMC 9	25.70±0.0313	0.039±0.0012	0.009±0.0004	2.0304
500 m away (West)	BMC 10	374.93±0.0313	0.066±0.0012	0.001±0.0004	28.9374
	Mean	200.32±0.0313	0.052±0.0012	0.005±0.0004	15.4839

Table 5a: Radiation Hazard parameters for soil samples within Location 1

Sample Code	D (nGy/hr)	AEDE (μSv/yr)	AGED (mSv/yr)	ELCR ($\times 10^{-3}$)	H _{ex}	H _{in}	I _γ
EMC 1	1.84	2.26	13.85	0.008	0.009	0.009	0.029
EMC 2	0.38	0.47	2.83	0.002	0.002	0.002	0.006
EMC 3	0.94	1.15	7.09	0.004	0.005	0.005	0.015
EMC 4	2.02	2.48	15.22	0.009	0.010	0.010	0.032
EMC 5	1.42	1.74	10.69	0.006	0.007	0.007	0.023
EMC 6	2.92	3.58	21.98	0.013	0.015	0.015	0.047
EMC 7	2.75	3.37	20.67	0.012	0.014	0.014	0.044
EMC 8	3.68	4.51	27.67	0.016	0.018	0.018	0.059
Mean	1.99	2.44	15.00	0.009	0.010	0.010	0.032

Table 5b: Radiation Hazard parameters for soil samples 500 m away from Location 1

Distance (m)	Sample Code	D (nGy/hr)	AEDE (μSv/yr)	AGED (mSv/yr)	ELCR ($\times 10^{-3}$)	H _{ex}	H _{in}	I _γ
500 m away (East)	EMC 9	1.90	2.33	14.32	0.009	0.009	0.009	0.054
500 m away (West)	EMC 10	1.58	1.94	11.90	0.008	0.008	0.008	0.045
	Mean	1.74	2.13	13.11	0.009	0.009	0.009	0.049

Table 6a: Radiation Hazard parameters for soil samples within Location 2

Sample Code	D (nGy/hr)	AEDE ($\mu\text{Sv/yr}$)	AGED (mSv/yr)	ELCR ($\times 10^{-3}$)	H _{ex}	H _{in}	I _y
BMC 1	3.23	3.96	24.32	0.014	0.016	0.016	0.091
BMC 2	1.10	1.35	8.23	0.005	0.005	0.006	0.031
BMC 3	3.43	4.21	25.85	0.015	0.017	0.017	0.097
BMC 4	3.00	3.68	22.57	0.013	0.015	0.015	0.085
BMC 5	3.28	4.02	24.72	0.014	0.016	0.016	0.093
BMC 6	2.93	3.59	22.06	0.013	0.015	0.015	0.083
BMC 7	3.38	4.15	25.45	0.015	0.017	0.017	0.095
BMC 8	2.92	3.58	21.97	0.013	0.015	0.015	0.083
Mean	2.91	3.57	21.89	0.012	0.015	0.015	0.082

Table 6b: Radiation Hazard parameters for soil samples 500 m away from Location 2

Distance (m)	Sample Code	D (nGy/hr)	AEDE ($\mu\text{Sv/yr}$)	AGED (mSv/yr)	ELCR ($\times 10^{-3}$)	H _{ex}	H _{in}	I _y
500 m away (East)	BMC 9	1.10	1.35	8.23	0.005	0.016	0.016	0.031
500 m away (West)	BMC 10	15.67	19.22	117.94	0.067	0.005	0.006	0.443
	Mean	8.38	10.28	63.08	0.036	0.011	0.011	0.237

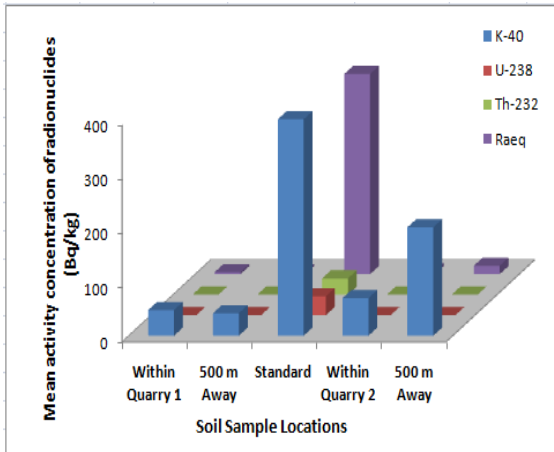


Figure 10. Mean activity concentrations of radionuclides in soils of the study area compared with the UNSCEAR, 2000.



Figure 11. A comparison of the absorbed dose rate (nGy/h) in soil of the study areas with the UNSCEAR, 2000.

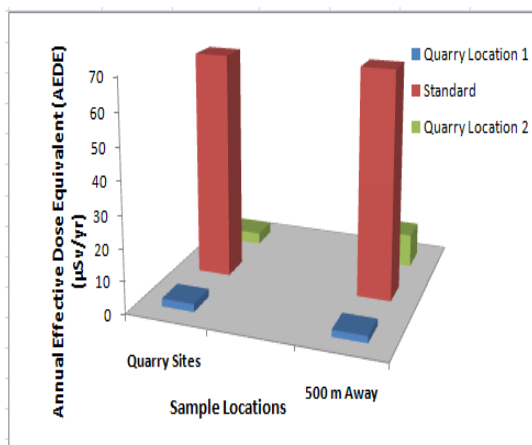


Figure 12. A comparison of the Annual Effective Dose Equivalent (outdoor) (AEDE) in soils of the study areas with the UNSCEAR, 2000.

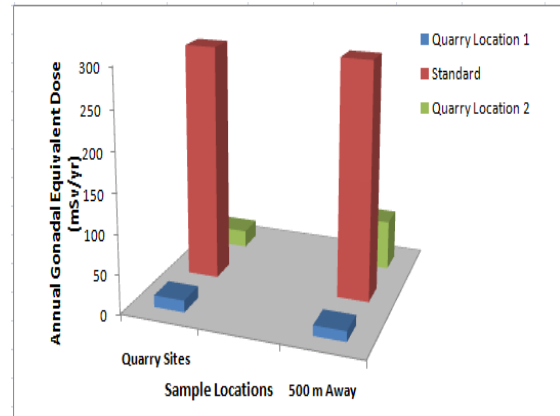


Figure 13. Annual Gonadal Equivalent Dose (AGED) in soils of the study areas compared with the UNSCEAR, 2000.

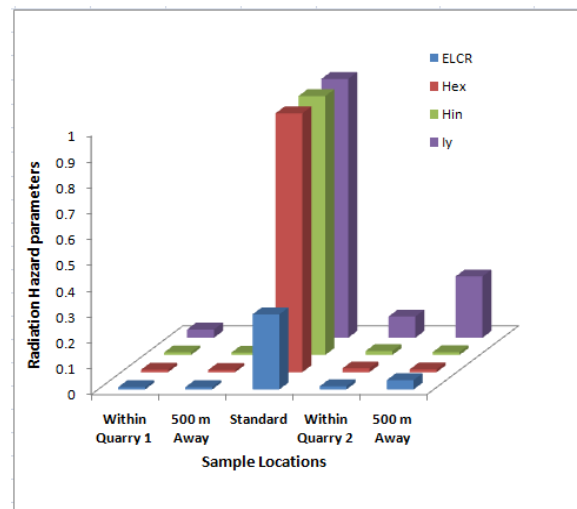


Figure 14. Excess Lifetime Cancer Risk, External hazard index, Internal hazard index and Gamma Representative Index in soils of the study areas compared with the UNSCEAR, 2000

5. CONCLUSION

The fact that quarry activities have the potential to increase the radiation dose received by individuals, radiometric survey has proved to be a useful tool in detecting the radiogenic emissions of most common radioactive elements in the study areas. The gamma count is a function of the concentration of radioactive elements in the rock. The higher values of radiation in the recently quarried coarse rock aggregates compared with the previously quarried coarse aggregate are an indication that radionuclides are resident in the parent rock materials. Also, relatively higher values of the radiations in the coarse aggregates of porphyritic granite gneiss compared with the coarse aggregates of fine to medium grained banded gneiss in this study implies that fine to medium grained rocks absorb and reflect radiation more easily than rocks of predominantly coarse grains. This shows that radionuclide level in rocks is influenced by grain size distribution.

The radioactivity concentrations of ^{238}U , ^{232}Th and ^{40}K in rock aggregates and soil samples of the two quarry sites showed that there are low level activities in the areas as they were far below their respective world standard values. The radionuclides are randomly distributed in the rock aggregates and soil with ^{40}K being the dominant radionuclide in the soils of the areas. The average dose rates and the annual effective dose equivalent calculated are very low compared to the world standard values for radiological hazard in humans. The other calculated radiation parameters (indices) including the excess lifetime cancer risk, radium equivalent, annual gonadal equivalent dose, representative gamma index, external and internal hazard indices for rock aggregates and soils of the areas are less than the world permissible value of unity. This indicates that interaction with the rock aggregates and soils do not expose the workers and the people within and around the areas to health problem. Generally, the relatively low gamma dose rates measured from the coarse rocks aggregate and subsurface soils of the two quarry sites show that quarry activities in the areas have not enhanced the background radiation level of the areas. This suggests that the rock aggregates and soils from these quarries can be used as building materials for housing and construction of roads without posing a health threat to the general public.

It is necessary to determine the radiation levels in and around quarries and different rock aggregates and soils before supply to the end users in construction works. This will definitely reduce the exposure of workers, users of such building materials and the populace to radionuclide radiations. This suggests that quarry activities need to be continuously monitored and workers occupancy in the quarry sites need to be controlled as exposure to the dose level over a long period can constitute serious health hazard especially to the quarry activities operators on the site and also the intake from inhaled and ingested radioactivity could present risks to workers and populace around the area. Based on this study, it is recommended that quarries must continuously be investigated of radiation level to ensure safety of lives of people and secure their health.

REFERENCES

- Awiri, G.O., Osimobi, J.O. and Agbalagba, E.O., 2012. Evaluation of radiation hazard indices and excess lifetime cancer risk due to natural radioactivity in soil profile of Udi and Ezeagu Local Government Areas of Enugu State, Nigeria. *Journal of Environmental and Earth Sciences*, 1(1), 1-10.
- Awiri, G.O., Egieya, J.M. and Ononugbo, C.P., 2013. Radiometric assay of hazard indices and excess lifetime cancer risk due to natural radioactivity in soil profile in Ogba/Egbama/Ndoni Local Government Area of Rivers State, Nigeria. *Academic Research International*, 4(5), 54-65.
- Beretka, J. and Mathew, P.J., 1985. Natural radioactivity of Australia building materials industrial wastes and by-products. *Health Physics*, 48, 87-95.
- Brimhal, W.H. and Adams, J.A.S., 1982. Concentration changes of thorium, uranium and metals in hydrothermally altered Conway Granite, New Hampshire. *Geochim, Cosmochim Acta*, 33, 130-131.
- David, O., 1998. Mining and quarrying occupational health and safety committee. Quarrysafe hazardous substances in quarries.
- Environmental Measurement Laboratory (EML) manual, 1983. Volchok, Herbert, L., dePlanque, Gail (Eds.), twenty-sixth ed. New York, US Department of Energy, Environmental Measurement Laboratory.
- Gunn, P., Minty, B. and Milligan, P., 1997b. The airborne gamma-ray spectrometric response over Arid Australian Terranes. In A. Gubins (Ed.), *Proceedings of Exploration 97: Fourth Decennial International Conference on Mineral Exploration*, Australia. 733-740.
- IAEA, 1991. Airborne gamma ray spectrometer surveying, International Atomic Energy Agency, Technical Report Series, No. 323, 97.
- IAEA, 2003. International Atomic Energy Agency (IAEA) guidelines for radioelement mapping using gamma ray spectrometry data, Vienna.
- James, L.W., 2013. Health hazards of mining and quarrying, safework_bookshelf. http://www.ilo.org/safework_bookshelf/English?content&nd=857170934.
- Milsom, J., 2003. *Field Geophysics: The geological field guide series*, John Milsom University College, London. Published by John Wiley and Sons Ltd. Third edition. 51-70.
- Montaj™ Tutorial, 2004. Two-Dimensional frequency domain processing of potential field data.
- Rahaman, M.A., 1989. Review of the basement geology of southwestern Nigeria. In: Kogbe, C.A., (ed) *Geology of Nigeria*, Rock View (Nig.) Limited, Jos, Nigeria. 39-56.
- Ramasamy, V., Suresh, G., Meenakshisundaram, V. and Gajendran, V., 2009. Evaluation of natural radionuclide content in river sediments and excess lifetime cancer risk due to gamma radioactivity. *Research Journal of Environmental and Earth Sciences*, 1(1), 6-10.
- Taskin, H., Karavus, M., Topuzoglu, A., Hindiroglu, S. and Karahan, G., 2009. Radionuclide concentrations in soil and lifetime cancer risk due to the gamma radioactivity in Kirklareli, Turkey. *Journal of Environmental Radioactivity*, 100, 49-53.
- Tim Driscoll, Steenland, K., Nelson, D.I. and James, L., 2004. *Environmental Burden of Disease Series*, No. 7; World Health Organization Protection of the Human Environment, Geneva.
- Tufail, M., Akhar, N., Jaried, S.A. and Hamid, T., 2007. Natural radiation hazard in building bricks fabrication from soils of two districts of Pakistan. *Radiological Protection*, 27, 481-492.

UNSCEAR, 2000. United Nations Scientific Committee on the Effects of Atomic Radiation. Sources, effects and risks of ionizing radiation. Report to the general assembly, annexes B: Exposure from natural radiation sources. New York. 678-679.

Veiga, R.G., Sanches, N., Anjos, R.M., Macario, K., Bastos, J., Iguatemy, M., Aguitar, J.G., Santos, M.A., Mosquera, B., Carvaiho, C., Baptista, M. and Umisedo, N.K., 2006. Measurement of natural radioactivity in Brazilian beach sands. *Radiation Measurements*, 41, 189-196.

Wilford, J., Bierwirth, P. and Craig, M., 1997. Application of gamma-ray spectrometry in soil or regolith mapping and applied geomorphology. *Journal of Australian Geology and Geophysics*, 17(2), 201-216.



*International Journal of Engineering and Geosciences (IJEG),
Vol; 3; , Issue; 1, pp. 036-042, February, 2018, ISSN 2548-0960, Turkey,
DOI: [10.26833/ijeg.373152](https://doi.org/10.26833/ijeg.373152)*

AUTOMATIC EXTRACTION OF BUILDING BOUNDARIES FROM HIGH RESOLUTION IMAGES WITH ACTIVE CONTOUR SEGMENTATION

Akbulut, Z., ^{1*} Özdemir, S., ¹ Acar, H., ² Dihkan, M., ² and Karsli, F., ²

¹Gumushane University, Engineering Faculty, Department of Geomatic Engineering, Gumushane, Turkey
(zeynepakbulut/samed.ozdemir @gumushane.edu.tr);

² Karadeniz Technical University, Engineering Faculty, Department of Geomatic Engineering, Trabzon, Turkey
(h_acar/mdihkan/fkarsli @ktu.edu.tr)

**ORCID ID 0000-0001-9801-1506; ORCID ID 0000-0001-7217-899X; ORCID ID 0000-0002-2954-7734;
ORCID ID 0000-0002-0027-236X; ORCID ID 0000-0002-0411-3315**

*Corresponding Author, Received: 30/12/2017, Accepted: 23/01/2018

ABSTRACT: Building extraction from remotely sensed images plays an important role in many applications such as updating geographical information system, change detection, urban planning, disaster management and 3D building modeling. Automatic extraction of buildings from aerial images is not an easy task because of background complexity, lighting conditions and vegetation cover that reduces separability or visibility of buildings. As a result, automatic building extraction can be a complex process for computer vision and image processing techniques.

In order to overcome this difficulty region-based active contour model was used to automatically detect the boundary of buildings for this study. To extract object boundaries, the model grows or shrinks the initial contour in the image. The main objective of this paper is making active contours algorithm perform without user interaction and to detect automatically initial contours to segment buildings with a software coded in Matlab. This task carried out by morphological operations, band ratio and thresholding methods. In this study, high resolution aerial images with 8 cm ground sampling distance (GSD) were used. Three separate test zones were selected with varying building level of detail on these images. Finally, it was assessed the accuracy of segmented buildings using Correctness, Completeness and Quality metrics by comparing the results images and manually digitized reference image.

The proposed approach for building extraction from images was shown to be 98% accurate on buildings with simple geometry and homogeneous roof textures. However accuracy of extracted buildings with heterogeneous roof textures and lighting, and complex geometry is 89%. The results clearly show that automatically calculated initial contour positions work in accordance with the active contour algorithm and easily extraction of the buildings boundaries.

Keywords: *Active Contour, Automatic, Building Extraction, High Resolution Image*

1. INTRODUCTION

The accurate segmentation of buildings from high resolution aerial images enables many useful applications such as change detection, disaster management, urban planning, updating geographic information system (GIS) databases. According to Wang (2016), extracting of buildings automatically from digital images has been an active research area in both photogrammetry and computer vision communities for decades. However, the automatic extraction of buildings from remotely sensed data is one of the challenging tasks faced by the computer vision and remote sensing communities (Siddiqui, et. al., 2016). This task is challenging due to many reasons such as complexity in the building structures, surrounding environment (highly-dense vegetation, occluded building and hilly scene), poor acquisition of data and registration error between data sources (Siddiqui, et. al., 2016). Also, this is because the remote sensing images are usually characterized by complex data in the form of heterogeneous regions with large intra-class variations and often lower inter-class variations (Alshehhi, et. al., 2017). Thereby automatic building boundary extraction with high accuracy is not a simple task because of background complexity, lighting conditions and vegetation cover that reduces separability or visibility of buildings.

Many researchers have presented methods for the segmentation of buildings from high resolution images. According to Attarzadeh and Momeni (2012), these algorithms have mainly considered radiometric, geometric, edge detection and shadow criteria approaches. Alshehhi et al. (2017) proposed a single patch-based Convolutional Neural Network (CNN) architecture for extraction of roads and buildings from high-resolution remote sensing data. Gilani et al. (2016) developed a methodology to extract and regularize buildings using features from point cloud and ortho-imagery. Wang (2016), developed an approach uses both geometric properties and radiometric properties of building to recognize buildings and delineate their boundaries. Wang's (2016) method consists of automatic generation of high quality point cloud from the imagery, building detection from point cloud, classification of building roof and generation of building outline. Turker and Koc-San (2015), developed an integrated approach for the automatic extraction of rectangular and circular shape buildings from high-resolution optical space borne images using the integration of support vector machine (SVM) classification, Hough transformation and perceptual grouping. Song et al. (2015) developed a method to extract buildings using LiDAR data. They based their method on distinct topological relationship and characteristics of contour lines and acquired promising results. Ghaffarian (2015) used active contours to segment buildings using automatically extracted initial contour positions based on shadow areas with region growing algorithm. However, the proposed method is incapable of detecting the buildings with no shadows. Kodors et al. (2015) used energy minimization approach to recognize buildings from LiDAR point cloud.

The extraction of 2D images from buildings in a dense urban area is an intricate problem due to the variety of shapes, sizes, colours, and textures (Ghanea et al., 2014). To overcome the problem, they proposed an algorithm which the core components are multispectral binary filtering, sub-clustering and single binary filtering, multi-conditional region growing and post-processing.

Awrangjeb et al., (2013), proposed a method for automatic 3D roof extraction through an effective integration of LiDAR (Light Detection And Ranging) data and multispectral ortho-imagery. Fazan and Poz (2013) used a method utilizing an energy function based on snakes that represents building roof contours in digital images and is optimized with a dynamic programming algorithm. Their results showed that the proposed method satisfactorily performed the task of extracting different building roof contours from digital images. However their method suffered from shadow and another roof nearby. Niveetha and Vidhya (2012) used mathematical morphologic operator to close and eliminate the undesired objects over the building roofs and extracted buildings based on the texture parameters from satellite imagery. Huang and Zuang (2012) proposed a systematic framework for building extraction from high-resolution imagery and aimed to enhance original morphological building index (MBI) algorithm. For this purpose they used a morphological shadow index (MSI) to detect shadows then geometrical index and a vegetation index are used to remove noise from narrow roads and bright vegetation. Ahmadi et al., (2010), proposed a modified active contour model to automatically extract building boundaries on aerial images. All building boundaries are detected by introducing certain points in the buildings' vicinity. They generated the initial curves automatically as a series of regular circles all over the image.

The main objective of this paper is making active contours algorithm perform without user interaction and detect initial contour positions automatically to segment buildings. To detect initial contour positions a series of morphological operations, band ratio and thresholding methods applied to images.

2. METHODOLOGY

The proposed approach to automate the active contour algorithm consists of three major steps. These steps are image pre-processing, initial contour creation and building extraction using active contours. Also it was created a Graphical User Interface (GUI) in Matlab software to evaluate all processes in a single frame, to find the optimum initial contour positions and maximum number of iterations, and to obtain the most accurate segmentation results for input image. The flowchart of the methodology for this study is shown in Figure 1 and Figure 2 represents the Matlab interface for the proposed algorithm.



Figure.1 Workflow of automatic building extraction with active contour segmentation

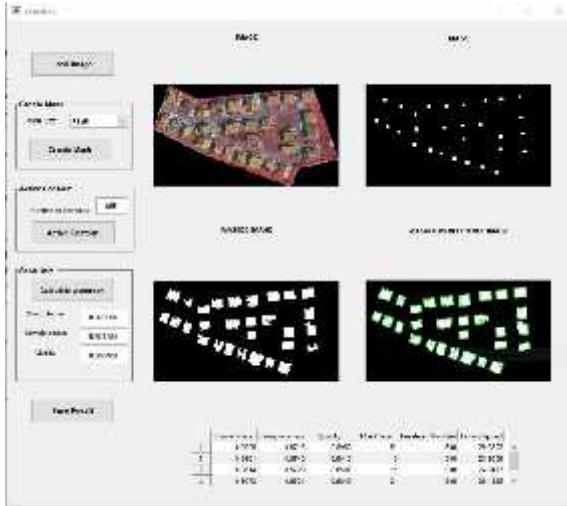


Figure.2 GUI created in Matlab

2.1 Active Contour Segmentation Algorithm

Active contours also called snakes was first proposed by Kass et al., (1988). The basic idea in active contour models or snakes is to evolve a curve, subject to constraints from a given image, in order to detect objects in that image. For instance, starting with a curve around the object to be detected, the curve moves toward its interior normal under some constraints from the image, and has to stop on the boundary of the object (Chan and Vese, 2001).

Active contour models can be classified into two categories: parametric snakes and geometrical snakes (Ahmadi et al., 2010). According to Ghaffarian (2015), there are three difficulties with the parametric model. First, the initial contour must, in general, be close to the true boundary, or else it will probably converge to the wrong result. Second, Snake active contours do not progress into boundary concavities. Third, parametric snake active contours are non-convex. Geometrical active contour models consist of two methods: edge based and region based. Region-based geometrical active contours rely on the homogeneity of spatially localized features such as gray level intensity, texture, and other pixel statistics (Ahmadi et al., 2010). Region based active contour models can detect details without significant edges and independent from object boundary waviness. Due to this advantages region based active contour model which also depends on Chan Vese Method is used.

Chan and Vese's (2001) method is a region based geometrical active contour model. The curve's motion is driven by a combination of internal and external forces, which achieve a minimal energy state when the curve/surface reaches the targeted image boundaries (Ahmadi et al., 2010). In Chan and Vese's method they added regularizing terms to the classical active contours to stop the evolving curve on the desired boundary. Energy function for active contour is shown in Eq. (1).

$$F_1(C) + F_2(C) = \int_{inside(C)} |u(x,y) - c_1|^2 dx dy$$

$$+ \int_{outside(C)} |u(x,y) - c_2|^2 dx dy \quad (1)$$

where C is the active contour curve, $u(x,y)$ is the pixel values of input image, c_1 and c_2 are illustrate the average of pixel values inside and outside of C , respectively (Chan and Vese, 2001; Ahmadi et al., 2010).

$$F_1(C) = \int_{inside(C)} |u(x,y) - c_1|^2 dx dy \quad (2)$$

$$F_2(C) = \int_{outside(C)} |u(x,y) - c_2|^2 dx dy \quad (3)$$

Equation (2) is internal energy of curve C and (3) is external energy of curve C . Chan and Vese (2001) noted that the boundary of the object C is the minimizer of the fitting energy:

$$\inf_C \{F_1(C) + F_2(C)\} \approx 0 \approx F_1(C) + F_2(C) \quad (4)$$

To explain this if the curve C is outside the object, then $F_1(C) > 0$ and $F_2(C) = 0$. If the curve C is inside the object, then $F_1(C) = 0$ but $F_2(C) > 0$. If the curve C is both inside and outside the object, then $F_1(C) > 0$ and $F_2(C) > 0$. Finally, the fitting energy will be minimized if the $C = C$, i.e. if the curve C is on the boundary of the object (Chan and Vese 2001).

In their active contour model Chan and Vese (2001), minimized fitting energy and added some regularizing terms as shown in Eq. (5);

$$F(C, c_1, c_2) = \mu \times \text{length}(C) + \nu \times \text{area}(\text{inside}C) + \lambda_1 \int_{inside(C)} |u(x,y) - c_1|^2 dx dy + \lambda_2 \int_{outside(C)} |u(x,y) - c_2|^2 dx dy \quad (5)$$

Regularizing terms include the length of curve C and/or the area inside C . In Eq. (5) μ , ν , λ_1 and λ_2 are fixed parameters and their values are $\mu \geq 0$, $\nu \geq 0$, $\lambda_1 > 0$ and $\lambda_2 > 0$. Finally, the minimizing problem can be expressed as follows;

$$\inf_C F(C, c_1, c_2) \quad (6)$$

2.2 Image Pre-processing

The proposed automatic building extraction approach was tested on high resolution color infrared aerial images. Spatial and radiometric resolution of these images is 8 cm and 12 bits, respectively. Test images include three different urban residential areas. First area contains 5 buildings with simple geometry and similar roof textures (Figure 3), second area includes 29 buildings with both relatively complex and simple geometry, and also with inhomogeneous roof textures and lighting. The other contains 27 buildings with complex geometry, texture and lighting with respect to second test area. One of the test areas was depicted in Figure 3.



Figure.3 Test area containing 5 buildings with similar geometric shapes. (a) original image, (b) decorrelation stretched image, (c) Gaussian smoothed image.

Before creating initial contour positions, images were required to be enhanced in order to achieve good results. First, the decorrelation stretch method was used to make the bands of the images more separable. After decorrelation stretching; vegetation, buildings and roads became more distinguished from each other. Images were smoothed to reduce textural details and color transitions. With these enhancements images can be processed with morphological operations more efficiently. After the enhancement operations a band ratio calculated in order to detect approximate building locations. Ratio image then converted to a binary image with Otsu's method. Binarized ratio results contained some undesirable pixel groups that could impair the mask creation process. These pixel groups were removed with a series of morphological operations such as opening and closing.

2.3 Automatic Creation of Initial Contour Position

Automatic extraction of buildings based on active contour algorithm was required automatic generation of initial contour positions using centers of points (x, y) which are candidate building pixels. The segmentation process starts at that initial contour positions. To create initial contour positions, firstly, some morphological operations were applied on binary images to separate background from foreground object and so candidate pixels correspondence with buildings were found. Then, pixels were labeled by scanning the imagery pixel by pixel with connected component analysis. After this operation, pixels were grouped by their unique label which is assigned to each class. The centroids (x, y) were calculated for each approximately detected building pixels group. Finally, all of the centroids were used as initial contour input for active contour segmentation by varying kernel (mask) sizes such as 5×5, 11×11, 21×21, and 51×51 pixels. Optimal kernel size can be selected by users for image segmentation on GUI. Figure 4 shows an example of scene for automatically detected centroids and initial contour positions in a test image.

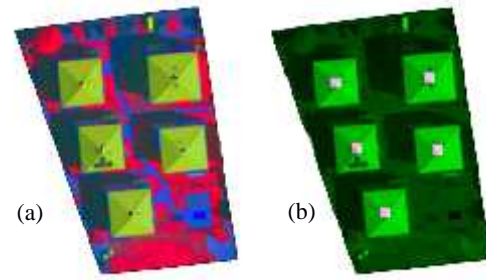


Figure.4 (a) automatically detected centroids (b) initial contour positions

2.4 Building Extraction with Active Contours

Active contour algorithm in Matlab requires the input arguments that are image to be segmented, initial contour positions (mask), maximum number of iterations and method. Input image is smoothed image as explain in section 2.2. Second input is initial contour mask mention in section 2.3. Third input is maximum number of iterations to perform in evolution of the segmentation, specified as a numeric scalar (URL-1, 2017). Active contour stops the evolution of the active contour when it reaches the maximum number of iterations (URL-1, 2017). Final input is region based Chan-Vese method that is describe in section 2.1. After preparing initial contours and recognize maximum iteration number image was segmented into two parts as background and foreground.

To accurately recognize boundaries of buildings is depend on well identified mask and maximum iteration number. Active contour also stops the evolution if the contour position in the current iteration is the same as the contour position in one of the most recent five iterations (URL-1, 2017). Optimum mask size and maximum number of iterations for input images were found by trial and error method on graphical user interface. Results images were filled with morphological operations.

Optional parameters for active contour algorithm in Matlab software are Smooth Factor and Contraction Bias. Smooth Factor is degree of smoothness or regularity of the boundaries of the segmented regions (URL-1, 2017). Contraction Bias is tendency of the contour to grow outwards or shrink inwards and this parameter does not guarantee that the contour contracts (or expands) (URL-1, 2017). For this reason, the default values of Contraction Bias and Smooth Factor were used in applying Chan-Vese method. Finally, output segmented binary image was obtained.

3. RESULTS AND DISCUSSION

The accuracy assessment of proposed approach were carried out by comparing automatically extracted buildings with manually digitized reference images using Completeness, Correctness and Quality metrics as shown in Eq (7), (8) and (9).

$$\text{Completeness} = \frac{|TP|}{|TP| + |FN|} \quad (7)$$

$$\text{Correctness} = \frac{|TP|}{|TP| + |FP|} \quad (8)$$

$$Quality = \frac{||TP||}{||TP||+||FN||+||FP||} \quad (9)$$

In Eqs. (7), (8), and (9), an entity classified as an object that also corresponds to an object in the reference is classified as a true positive (TP). A false negative (FN) is an entity corresponding to an object in the reference that is classified as background, and a false positive (FP) is an entity classified as an object that does not correspond to an object in the reference. A true negative (TN) is an entity belonging to the background both in the classification and in the reference data (Rutzinger et al. 2009; Shufelt 1999; Karsli et al. 2016).

The results of automatically extracted building boundaries were shown in Figs. (5), (6) and (7). Quantitative results for each test area were depicted in Table (1), (2) and (3).



Figure.5 Results of first test area

Table 1 Accuracy assessment of first region with 5 buildings

Correctness	Completeness	Quality	Mask size	Iteration
0,872	0,995	0,868	5×5	200
0,889	0,994	0,884	11×11	200
0,918	0,993	0,912	21×21	200
0,981	0,990	0,971	51×51	200
0,970	0,990	0,960	5×5	250
0,975	0,990	0,966	11×11	250
0,984	0,989	0,973	21×21	250
0,989	0,987	0,977	51×51	250
0,989	0,987	0,977	5×5	300



Figure.6 Results of second test area

Table 2 Accuracy assessment of second region with 29 buildings

Correctness	Completeness	Quality	Mask size	Iteration
0.818	0.974	0.801	5×5	500
0.871	0.973	0.851	11×11	500
0.907	0.972	0.885	21×21	500
0.921	0.971	0.896	51×51	500
0.922	0.971	0.897	51×51	750
0.922	0.971	0.898	51×51	1000



Figure.7 Results of third test area

Table 3: Accuracy assessment of third region with 27 buildings

Correctness	Completeness	Quality	Mask size	Iteration
0.871	0.966	0.845	5×5	500
0.883	0.965	0.856	11×11	500
0.892	0.965	0.864	21×21	500
0.915	0.963	0.884	51×51	500
0.923	0.961	0.890	11×11	750
0.923	0.961	0.890	51×51	750
0.923	0.961	0.890	21×21	1000
0.923	0.961	0.890	11×11	1000
0.923	0.961	0.890	51×51	1000

According to the results, optimum parameter values were determined with various combinations of maximum number of iterations and initial contour size for each test area to increase the accuracy of automatic building extraction. The trials were terminated when there is no improvement over optimum values. For instance, after performing active contour segmentation with 11×11 initial contour size and 750 iterations, results compared to other segmentations which carried out with greater values for iteration number and initial contour size showed no significant improvement as shown in Table 3. Moreover in Table 1, same results were acquired both 51×51 initial contour size with 250 iterations and 5×5 initial contour size with 300 iterations. As a result, selecting small initial contour size with a suitable iteration number can give the same results with a bigger initial contour size and lower iteration number.

To get desired segmentation results, there is no need to initial contour positions be close the object boundaries. Therefore, an initial contour selected at the center of the object to be segmented can be sufficient. Thus, high segmentation accuracy can be acquired with small initial contour created near the object center and a greater number of iteration. Accuracy for each test area was shown in Table 4.

Table 4 The best results for each test area

Test Areas	Correctness	Completeness	Quality
First	0,989	0,987	0,977
Second	0,922	0,971	0,898
Third	0,923	0,961	0,890

While spectrally inhomogeneous and geometrically complex buildings were extracted with lower accuracy (Fig. 8 and 9), but buildings with spectrally homogeneous roof were extracted with higher accuracy (fig. 10). The reason for low extraction accuracy depends on the objects like solar panels or windows locating near the roof edges and in such situation active contour algorithm.

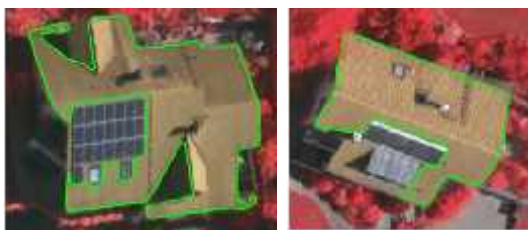


Figure.8 Objects on roofs such as sun panels affect the accuracy of active contours



Figure.9 Shadowed zones on roofs especially near the edge also impair active contours, spectrally indistinctive pixels mixed with roof pixels



Figure.10 Decently illuminated roofs without prominent shadow areas can be accurately extracted by active contours, simple roof shapes can be extracted easily

4. CONCLUSIONS AND FUTURE WORKS

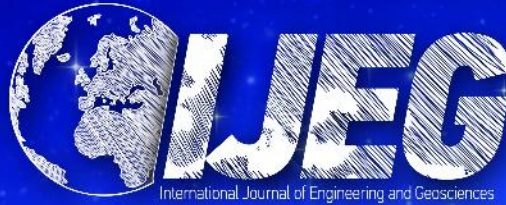
This study presents to create automatic initial contour positions for the extraction of buildings from high resolution aerial images instead of manually defining the initial contour positions in region based active contour algorithm. To do so, first the building candidate pixels were determined with morphological operations and labeled as the regions of building from binary images. Then, each building candidate pixel group's centroids were calculated. These centroids were used as initial contour positions by upsizing their dimensions with predetermined values such as 5×5 , 11×11 , 21×21 , and 51×51 to run active contour model. To obtain desirable segmentation results, trial and error approach were implemented to find optimum initial contour size and iteration number in GUI.

With the proposed approach, all of the buildings were extracted from images. However, shadow effects and mixed pixels couldn't be avoided due to spectral characteristics of the environment such as roads and vegetation. As a result of previously mentioned issues, some of the detected buildings have jagged boundaries because of shadow effects and some of the building boundaries expanded to non-building areas with spectrally similar characteristics. Also, if the initial curve overlaps with a chimney, window or a solar panel then the curve created by active contour algorithm retracts inward and disappear. To overcome this problem, initial curve size must be large enough to surround such objects. Nevertheless for homogeneous surfaced building roofs, overall segmentation quality does not affected by the size of initial contour.

Because of the fact that the main contribution in this study is to automatically create initial contour positions, it was not taken into consideration of the shadow regions and smoothness of the boundaries. Thus, as a future work we are going to smooth jagged boundaries and remove shadows effects on building roofs. Also, it is consider that Digital Elevation Model (DEM) covering the images will be included into dataset as a one layer to extract building boundaries with different roof textures and colors with active contour algorithm.

REFERENCES

- Ahmadi, S., Zoj, M. J. V., Ebadi, H., Moghaddam, H. A., Mohammadzadeh, A., 2010, Automatic urban building boundary extraction from high resolution aerial images using an innovative model of active contours, *International Journal of Applied Earth Observation and Geoinformation*, 12 (2010) 150–157.
- Alshehhi, R., Marpu, P. R., Woon, W. L., Mura, M. D., 2017, Simultaneous extraction of roads and buildings in remote sensing imagery with convolutional neural networks, *ISPRS Journal of Photogrammetry and Remote Sensing*, 130 (2017) 139–149.
- Attarzadeh, R., Momeni, M., 2012, Object-Based Building Extraction from High Resolution Satellite Imagery, *International Archives of the Photogrammetry, Remote Sensing and Spatial Information Sciences*, Volume XXXIX-B4, 2012 XXII ISPRS Congress, 25 August – 01 September 2012, Melbourne, Australia.
- Awrangjeb, M., Fraser, C. S., Lua, G., 2013, Integration of Lidar Data And Orthoimage For Automatic 3D Building Roof Plane Extraction, *Multimedia and Expo (ICME)*, 2013 IEEE International Conference on, doi: 10.1109/ICME.2013.6607612.
- Chan, T. F. and Vese, L. A., 2001, Active contours without edges, *IEEE Transactions on Image Processing*, Volume 10, Issue 2, pp. 266-277.
- Fazan, A. J., Poz, A. P. D., 2013, Rectilinear building roof contour extraction based on snakes and dynamic programming, *International Journal of Applied Earth Observation and Geoinformation*, doi: 10.1016/j.jag.2013.03.003.
- Ghaffarian, S., 2015, An Approach For Automatic Building Extraction From High Resolution Satellite Images Using Shadow Analysis And Active Contours Model, Master Thesis, Hacettepe University, Ankara, Turkey.
- Ghanea, M., Moallem P., Momeni, M., 2014, Automatic Building Extraction in Dense Urban Areas through GeoEye Multi-Spectral Imagery, *International Journal of Remote Sensing* 35 (13): 5094–5119. doi:10.1080/01431161.2014.933278.
- Gilani, S. A. N., Awrangjeb, M., Guojun, L., 2016, An Automatic Building Extraction and Regularisation Technique Using LiDAR Point Cloud Data and Orthoimage, *Remote Sensing* 2016, 8(3), 258, doi: 10.3390/rs8030258.
- Huang, X., Zhang, L., 2012, Morphological Building/Shadow Index for Building Extraction From High-Resolution Imagery Over Urban Areas, *IEEE Journal of Selected Topics in Applied Earth Observations and Remote Sensing*, Volume: 5, Issue: 1, Feb. 2012, doi: 10.1109/JSTARS.2011.2168195.
- Karsli, F., Dihkan, M., Acar, H., Ozturk, A., 2016, Automatic building extraction from very high-resolution image and LiDAR data with SVM algorithm, *Arabian Journal of Geosciences*, doi: 10.1007/s12517-016-2664-7.
- Kass, M., Witkin, A., Terzopoulos, D., 1988, Snakes: Active contour models, *International Journal of Computer Vision*, 321-331.
- Kodors, S., Ratkevics, A., Rausis, A., Buls J., 2015, Building Recognition Using LiDAR and Energy Minimization Approach, *Procedia Computer Science*, Volume 43, 2015, Pages 109-117.
- Niveetha, M. A., Vidhya, R., 2012, Automatic Building Extraction Using Advanced Morphological Operations and Texture Enhancing, *Procedia Engineering* 38:3573-3578.
- Rutzinger, M., Rottensteiner, F., Pfeifer, N., 2009, A comparison of evaluation techniques for building extraction from airborne laser scanning, *IEEE Journal of Selected Topics in Applied Earth Observations and Remote Sensing* 2(1):11–20.
- Siddiqui, F. U., Teng, S. W., Awrangjeb, M., Lu G., 2016, A Robust Gradient Based Method for Building Extraction from LiDAR and Photogrammetric Imagery, *Sensors* 2016, 16(7), 1110; doi:10.3390/s16071110.
- Song, J., Wu, J., Jiang, Y., 2015, Extraction and reconstruction of curved surface buildings by contour clustering using airborne LiDAR data, *Optik* 126 (2015), 513–521.
- Shufelt, J. A., 1999, Performance evaluation and analysis of monocular building extraction from aerial imagery. *Pattern Analysis and Machine Intelligence*, *IEEE Transactions on* 21(4):311–326.
- Turker, M., Koc-San, D., 2015, Building extraction from high-resolution optical spaceborne images using the integration of support vector machine (SVM) classification, Hough transformation and perceptual grouping, *International Journal of Applied Earth Observation and Geoinformation*, 34 (2015) 58–69.
- URL-1, 2017, <https://www.mathworks.com/help/images/ref/activecontour.html>, [12 November 2017].
- Wang, Y., 2016, Automatic Extraction of Building Outline From High Resolution Aerial Imagery, *The International Archives of the Photogrammetry, Remote Sensing and Spatial Information Sciences*, Volume XLI-B3, 2016 XXIII ISPRS Congress, 12–19 July 2016, Prague, Czech Republic.



International Journal of Engineering and Geosciences (IJEG) is tri-annual journal. It covers all aspects and information on scientific and technical advances in the geomatic sciences.

AIM AND SCOPE

IJEG publishes original and innovative contributions in geomatics applications ranging from the integration of instruments, methodologies and technologies and their use in the environmental sciences, engineering and other natural sciences. Geomatics is a branch which is applied widely in many other areas, this journal aims to cover the entire vertical of Geomatics, Geosciences including its application domains. The areas covered in the journal includes

Photogrammetry

Remote Sensing

Geographical Information systems

Geodesy sciences

Land Management

Surveying

Cartography

Unmanned aerial vehicles applications for mapping

Close range photogrammetry applications

Lidar

Terrestrial laser scanning application

Parameter estimation and modelling

Agricultural application of Gps, Gis and Remote sensing

And all Application of Geomatics